CHAPTER THREE

Quantum transport study in three-dimensional topological insulator $BiSbTeSe_2$

Yang Xu[a] **and Yong P. Chen**[b,c,d,e,f,g,h,*]

[a]Beijing National Laboratory for Condensed Matter Physics and Institute of Physics, Chinese Academy of Sciences, Beijing, China
[b]Department of Physics and Astronomy, Purdue University, West Lafayette, IND, United States
[c]Birck Nanotechnology Center, Purdue University, West Lafayette, IND, United States
[d]Purdue Quantum Science and Engineering Institute, Purdue University, West Lafayette, IND, United States
[e]Quantum Science Center, Oak Ridge, TN, United States
[f]School of Electrical and Computer Engineering, Purdue University, West Lafayette, IND, United States
[g]Institute of Physics and Astronomy and Villum Centers for Dirac Materials and for Hybrid Quantum Materials, Aarhus University, Aarhus-C, Denmark
[h]WPI-AIMR International Research Center for Materials Sciences, Tohoku University, Sendai, Japan
[*]Corresponding author: e-mail address: yong.chen@purdue.edu

Contents

Semiconductors and Semimetals, Volume 108
ISSN 0080-8784
https://doi.org/10.1016/bs.semsem.2021.07.002

1. Introductions

1.1 Brief introduction to topological states of matter

For a long period, principles of symmetry breaking have been successful in classifying most of the states of matter. However, the discovery of quantum Hall effect (QHE) in the 1980s brought a new paradigm for studying topology and symmetry protected topological states in condensed matter systems (Klitzing et al., 1980; Thouless et al., 1982). In the QHE, the Hall conductance of a two-dimensional electron gas (2DEG) is precisely quantized into integer multiples of e^2/h ($\sim 1/25812.8\,\Omega^{-1}$), insensitive to the sample geometry or microscopic details of the material. The QHE has been used as a resistance metrology and the determination of fundamental constants. The precise quantization of the Hall signal can be understood by the fact that it is topological states of matter characterized by a topological invariant, so-called Chern number or Thouless–Kohmoto–Nightingale–Nijs (TKNN) number (Thouless et al., 1982). In a topological phase, certain fundamental properties, such as the quantized Hall conductance or the number of edge modes (equal to Chern number) in a QHE, are independent of material details and insensitive to smooth deformation of the system (such as small density change or disorders) unless the system passes through a quantum phase transition.

Since the proposals of quantum spin Hall effect (Bernevig and Zhang, 2006; Kane and Mele, 2005), many new materials belonging to different topological classifications have been theoretically predicted and experimentally verified. Typical examples are 2D and 3D topological insulators (TIs), topological crystalline insulators, and topological Dirac/Weyl semimetals (Armitage et al., 2018; Dziawa et al., 2012; Fu, 2011; Hasan and Kane, 2010; Qi and Zhang, 2011). Recent high-throughput searches give a catalogue of more than a thousand of topological materials (Tang et al., 2019; Vergniory et al., 2019). Different from the QH states that need magnetic field to explicitly break the time-reversal symmetry, the 2D and 3D TIs belong to a class that is invariant under time reversal, where spin-orbit coupling (SOC) and band inversion play essential roles. While the bulk remains gapped, helical and non-trivial edge/surface states emerge near the boundary of a 2D/3D TI.

The revelation of topological Dirac and Weyl semimetals have broadened the classification of topological phases of matter beyond insulators (Armitage et al., 2018). The Dirac semimetal is a natural 3D counterpart of graphene, possessing 3D Dirac fermions in the bulk. In other words, the energy bands disperse linearly along all (three) momentum direction, with the conduction bands touching the valence bands only at the Dirac point. The 3D Dirac fermion in a Dirac semimetal is composed of two overlapping Weyl fermions (chiral massless particles) that has opposite chirality and can be separated in momentum space if either time-reversal or inversion symmetry is broken, resulting in a Weyl semimetal. Interestingly, the surface states of a Dirac/Weyl semimetal take the form of Fermi arcs connecting the projection of bulk Dirac/Weyl nodes in the surface Brillouin zone. Dirac semimetals include materials such as Na_3Bi and Cd_3As_2 (Liu et al., 2014a,b). Weyl semimetals are such as TaAs (Lv et al., 2015; Xu et al., 2015).

The Dirac/Weyl semimetal phase could also exist near the topological phase transition from a band insulator to a 3D TI by breaking symmetries at the critical point (Liu et al., 2014a). Or a Weyl semimetal can be constructed by stacking thin films of magnetically doped 3D TIs (Burkov and Balents, 2011). This provides a way in realizing Weyl semimetals from the tuning phase transitions in a 3D TI. A 2D topological semimetal (TSM) phase has been predicted to be induced by an in-plane magnetic field in thin 3D TIs with hybridization gap opening (Burkov and Balents, 2011). The in-plane magnetic field plays a role to split and separate the top and bottom surface Dirac points in the momentum space and prohibit their mutual annihilation, resulting in the 2D TSM phase that provides a 2D analogue of Weyl semimetals (even though strictly speaking Weyl fermions cannot be defined in even spatial dimensions (Armitage et al., 2018)).

1.2 Introduction to 3D topological insulators

A 3D TI is characterized by an insulating bulk band gap and gapless conducting topological surface states (TSS) of spin-helical massless 2D Dirac fermions. The conducting edge in a 3D TI is a closed 2D surface (while in a 2D TI it is a 1D edge channel). Simple versions of 3D TI materials have been first found in Bi_xSb_{1-x} (x in certain range), Bi_2Se_3, Bi_2Te_3 and

Sb_2Te_3, all of which are considered to be prototypical 3D TIs (Hasan and Kane, 2010; Qi and Zhang, 2011). Historically those bismuth/antimony based chalcogenides have been studied for a long time but mostly from the perspective of thermoelectric properties (Heremans et al., 2017; Nolas and Jeffrey Sharp, 2013). Only until recent years has their profile as a 3D TI been discovered. 3D TI has also been reported in strained HgTe (Brüne et al., 2011). There are also some other types of TI candidates such as SmB_6 and ternary Heusler compounds (Chadov et al., 2010; Wolgast et al., 2013). The 3D TI provide a novel playground for realizing potential applications and intriguing physics. For example, the spin-momentum locking of the TSS promises for current-driven spintronics. A magnetic gap on the surface state can lead to an exotic quantum anomalous Hall state and topological magnetoelectric effect (Chang et al., 2013; Qi et al., 2008; Yu et al., 2010). The TSS in proximity with s-wave superconductors would lead to a state that supports Majorana fermions, which have the potential for building topological quantum computers (Fu and Kane, 2008).

The experimental demonstration of 3D TIs was first done by angle-resolved photoemission spectroscopy (ARPES) method (Hasan and Kane, 2010). The ARPES data clearly resolved the spin-polarized Dirac cone. However, the prototypical 3D TIs (such as Bi_2Se_3, Bi_2Te_3) are usually suffering from unintentional impurity doping, in which bulk carriers unavoidably present and overwhelm the topological surface states (TSS) in transport studies. There are a lot of efforts trying to lower the bulk contribution to observe truly TSS dominated transport signatures. Several strategies are commonly applied. (1) Chemical doping, such as adding Ca substitution for Bi in Bi_2Se_3 to compensate the electrons created by Se vacancies (Hor et al., 2009). (2) Lowering the surface to bulk ratio, such as fabricating thin film and nanostructures. (3) Electrical gating (Chen et al., 2010). Through these efforts, people have been able to observe for example, weak-antilocalization (Chen et al., 2010), Shubnikov-de Haas (SdH) oscillations (Analytis et al., 2010; Qu et al., 2010) and an ambipolar electric field effect (Kong et al., 2011) arising from the TSS. An example of developing QHE from TSS has only been reported in strained HgTe (Brüne et al., 2011).

1.3 Introduction to an intrinsic 3D TI $BiSbTeSe_2$

After initial attempts in reducing bulk carriers of binary compounds, ternary and quaternary tetradymite TI materials such as Bi_2Te_2Se and

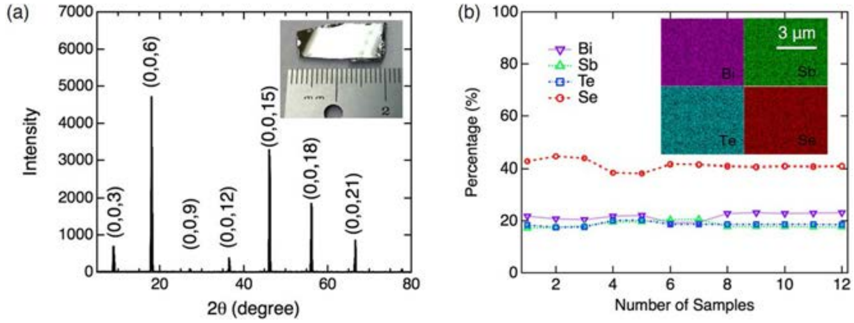

Fig. 1 (A) XRD measured on a BSTS crystal. (B) Molar percentage of Bi, Sb, Te, Se in 12 different samples measured by EDS. Inset is an example of the EDS mappings in a small area.

$Bi_{2-x}Sb_xTe_{3-y}Se_y$ have been found to exhibit large bulk resistivity and more intrinsic behaviors (Arakane et al., 2012; Ren et al., 2010; Taskin et al., 2011; Xia et al., 2013; Xiong et al., 2012b). Here, "intrinsic" means "compensated" (a terminology commonly used for describing undoped semiconductors) and the bulk carriers should freeze out at low temperatures. High-quality single crystals of $BiSbTeSe_2$ (BSTS) have been grown by vertical Bridgman method. Various material characterizations are performed on the BSTS crystals, including X-ray diffraction spectrum (Fig. 1A), elemental energy-dispersive X-ray spectroscopy (Fig. 1B), ARPES (Fig. 2), and scanning tunneling spectroscopy (see the results elsewhere (Xu et al., 2014)), all in good agreement with previous measurements in this material system. They indicate that the BSTS is promising for observing surface-dominant transport properties, which will be presented in the following sections.

2. Electrical properties of $BiSbTeSe_2$

2.1 Sample preparation

In order to perform electrical transport measurements on BSTS, we fabricated samples into two forms, bulk samples and relatively thin devices. The bulk samples (thickness > 1 μm) are cleaved from the bulk crystal with razor blades and then cut into rectangular shapes, followed by making electrical connections with multiple indium contacts and gold wires (Fig. 3A). The thicknesses of bulk samples are measured by taking an optical image of the cross section under a microscope. Thinner flakes (<~500 nm)

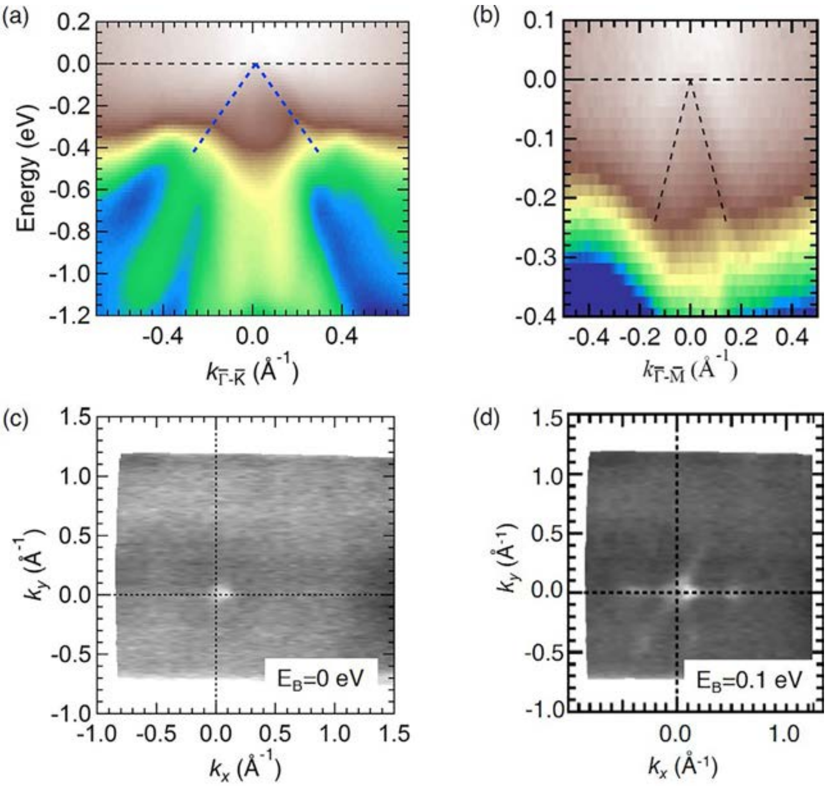

Fig. 2 Band structure and Fermi surface of BSTS measured by ARPES. Energy resolution was set to ~20 meV. Samples were cleaved in situ and measured at 20 K under a vacuum condition better than 4×10^{-11} Torr. (A and B) The measured band structure (binding energy *E* vs momentum *k* map) of BSTS along $\bar{\mathrm{K}}$-$\bar{\Gamma}$-$\bar{\mathrm{K}}$ (A) and $\bar{\mathrm{M}}$-$\bar{\Gamma}$-$\bar{\mathrm{M}}$ (B) directions, respectively. The blue dashed lines are guides to the eye to highlight the linearly dispersive Dirac TSS in the bulk band gap, with the Fermi level (E_F) indicated by the horizontal black dashed line. (C and D**)** The Fermi surface map of BSTS measured at the Fermi energy (C) and binding energy of 0.1 eV (D). The point-like Fermi surface in (C**)** indicates that E_F is located very close to the Dirac point of TSS. The star-like features in (D) are associated with bulk valence band.

are mechanically exfoliated onto Si substrates (with 300-nm-thick SiO_2 coating) by a typical "Scotch tape" method (exploited for the discovery of monolayer graphene) (Novoselov et al., 2004). The thickness of a nanoflake is measured by atomic force microscopy (AFM). The Cr/Au electrodes for the device with exfoliated flakes are defined by standard electron-beam lithography and metal evaporation (see Fig. 3B).

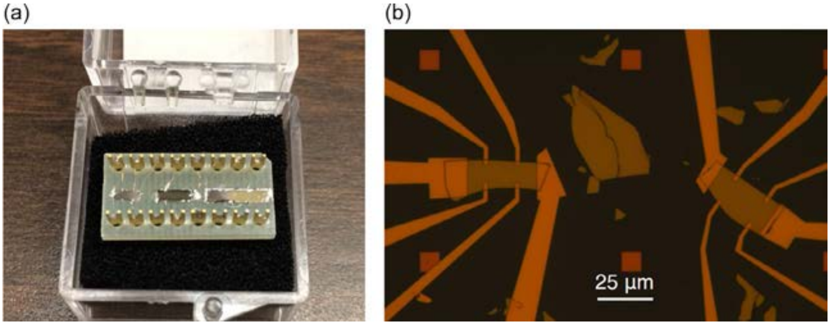

Fig. 3 (A) An image of three BSTS bulk devices with indium contacts on a 16-pin chip carrier for electrical transport measurements. (B) An image taken under an optical microscope of two BSTS flake devices.

Both types of devices have a six terminal quasi-Hall-bar geometry. Four-terminal longitudinal (R_{xx}) and Hall (R_{xy}) resistances were measured with the standard lock-in technique and low-frequency (<20 Hz) excitation current of 1 μA (bulk samples) or 100 nA (thin flake devices). Then we can extract the corresponding 2D resistivities $\rho_{xx} = R_{xx} * (W/L) = R_{sh}$ (with R_{sh} being the sheet resistance, W and L the channel width and length for the quasi-Hall-bar devices), $\rho_{xy} = R_{xy}$, and conductivities $\sigma_{xx} = \rho_{xx}/(\rho_{xx}{}^2 + \rho_{xy}{}^2)$, $\sigma_{xy} = \rho_{xy}/(\rho_{xx}{}^2 + \rho_{xy}{}^2)$ from tensor inversion.

2.2 Extracting conduction for the surface states

We first discuss transport measurements performed at zero magnetic field ($B = 0$ T) on BSTS samples with various thicknesses (t). Fig. 4A shows the temperature (T) dependence of the sheet resistance R_{sh} in five selected samples. The thicker samples (e.g., $t = 37$ μm) exhibit an insulating behavior (attributed to the bulk) at high T and a saturating and weakly metallic behavior (attributed to the residual metallic surface conduction after bulk carriers freeze out) at low T. As t (thus the bulk portion) is reduced (e.g., $t = 160$ and 480 nm), the bulk-insulating behavior weakens and moves to higher T, while the T range for the low-T metallic conduction expands. For thinnest samples ($t = 20$ nm), R_{sh} is relatively T-insensitive and metallic over the entire T range measured. We also note that while R_{sh} (attributed to the bulk) at high T (>~250 K) is strongly thickness-dependent (from <10 to >2 kΩ), R_{sh} (attributed to the surface) at low T (<50 K) reaches comparable values (a few kΩ) for all the samples despite the three orders of magnitude variation in their thickness (Fig. 4B).

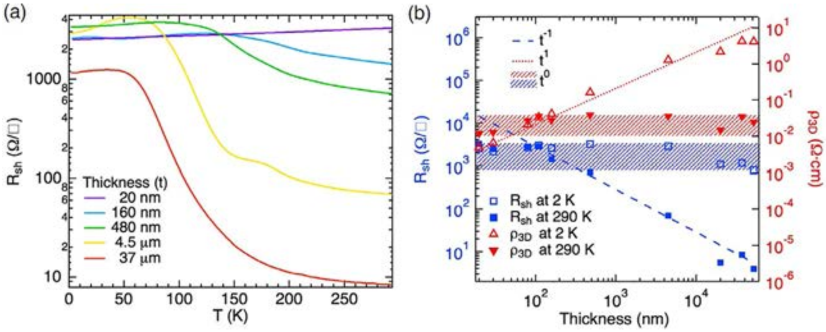

Fig. 4 (A) Sheet resistance (R_{sh}) measured at zero magnetic field vs temperature (T) in five devices with different thicknesses. (B) R_{sh} and 3D resistivity $\rho_{3\mathrm{D}}$ as functions of sample thickness at two typical temperatures. At $T=2$ K, the sheet resistance exhibits a 2D behavior (relatively insensitive to the thickness, highlighted by the blue horizontal band). The dashed line and red horizontal band represent expected behaviors for R_{sh} and $\rho_{3\mathrm{D}}$ of a 3D bulk conductor (our data at 290 K exhibited such 3D behavior for samples thicker than $>\sim$00 nm).

In order to more quantitatively extract the surface contribution to the total conductance (G_{tot}), we fit our $R_{\mathrm{sh}}(T)$ data to a simple model (Gao et al., 2012), where the total (sheet) conductance $G_{\mathrm{tot}}(T)=1/R_{\mathrm{sh}}(T)$ is the parallel sum of a thermally activated bulk conductance $G_b(T)=t^*(\rho_{b0}e^{\Delta/k_BT})^{-1}$ (where k_{B} is the Boltzmann constant and the fitting parameters $\rho_{\mathrm{b}0}$ is the high temperature bulk resistivity and Δ is the activation energy) and a metallic surface conductance $G_{\mathrm{sur}}(T)=(R_{\mathrm{sh}0}+A^*T)-{}^{1}$ (where fitting parameters $R_{\mathrm{sh}0}$ represents a low-T residual resistance due to impurity scattering and A reflects the electron-phonon scattering) (Giraud et al., 2012; Novoselov et al., 2004). This model gives reasonably good fits to most samples over the full temperature range, and extract the surface conductance G_{sur} for samples with different thickness (Fig. 5). In few samples (e.g., see Fig. 5A, $t=80$ nm), the fitting is excellent from 300 K down to 50 K, but would not account for a small resistance peak at lower T (~30 K, where the fit underestimates the data by up to 10%). This peak might be due to a small part of the sample insulating with a thermal activation gap smaller than the main bulk activation gap. Each curve was fitted multiple times over different ranges of temperatures to calculate approximate confidence intervals and error bars (Fig. 5B and C). For each fitting parameter, the values for all samples (with widely-varying thickness) are found to be on the similar order of magnitude. For example, A ranges mostly from 1 to 8 Ω/K (average 6 Ω/K), comparable with a previous measured 3 Ω/K in $\mathrm{Bi_2Se_3}$ (Kim et al., 2012b).

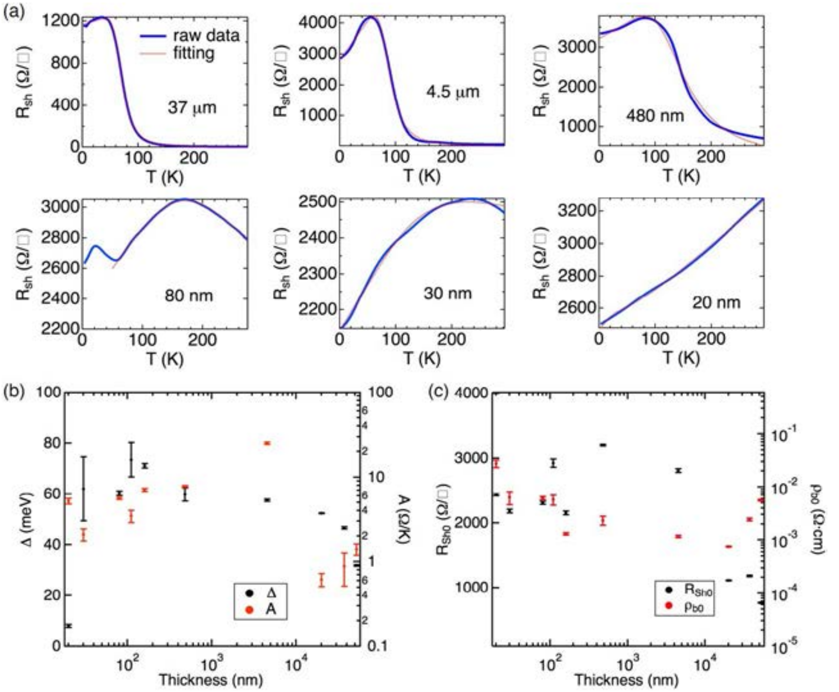

Fig. 5 (A) Fitting for R_{sh} vs temperature (T) in six selected samples, using the two channel (metallic surface + activated bulk) model described in the maintext. (B) and (C) show the fit parameters with corresponding error bars with 95% confidence level for all the 10 samples studied. Note some fitting have small error bars barely distinguishable in the current y-axis scale. The bulk channel fitting parameters Δ and ρ_{b0} from the 20-nm-thick sample deviate more from the others likely because the sample is too thin to accurately extract the bulk contribution.

Fig. 6A shows the ratio (G_{sur}/G_{tot}) between the fitted G_{sur} and the measured total conductance G_{tot} as a function of thickness (t) at three representative temperatures. At low T (50 K or below), the surface contribution to the total conductance is nearly 100% for all the samples (with thickness from <100 nm to >10 μm). Remarkably, in thinner samples ($t < 100$ nm) the surface conduction can exceed the bulk conduction with $G_{sur}/G_{tot} > 60\%$ even at room temperature ($T = 290$ K).

The averaged fitting parameters (between all samples) $\rho_{b0} = (3.5 \pm 0.8) \times 10^{-3}\,\Omega\cdot$cm, $\Delta = 57 \pm 4$ meV, $R_{sh0} = 2.0 \pm 0.3$ kΩ, $A = 6 \pm 2\,\Omega$/K can be taken as representative material parameters for BSTS to predict G_{sur}/G_{tot} for any given thickness and temperature, as shown in the 2D color plot in Fig. 6B. We see that surface-dominant transport with (G_{sur}/G_{tot} >80%) can be achieved in moderate low T (<50 K) for samples up to

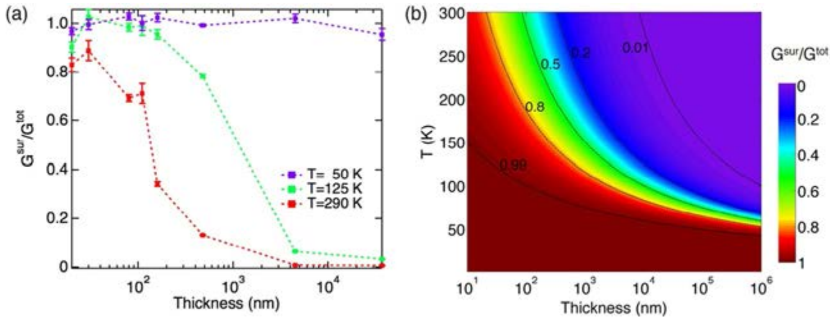

Fig. 6 (A) Surface to total conductance ratio (G_{sur}/G_{tot}) as a function of the sample thickness at three representative temperatures. Here G_{tot} is the measured conductance and G_{sur} is extracted from fitting the measured R_{sh} vs T. (B) Predicted G_{sur}/G_{tot} (shown in color scale) for our BSTS as a function of temperature and sample thickness. Here G_{sur} and G_{tot} are calculated based on the bulk and surface conductivities averaged from multiple measured devices. Black dashed curves are contours for a few G_{sur}/G_{tot} values.

macroscopic thickness of 1 mm, or in thin (tens of nm) samples up to room temperature ($300K$) in this material system. The extracted bulk thermal activation energy Δ is larger than $2k_BT$ for $T = 300\,\mathrm{K}$, which enables surface-dominant transport at room temperature. We also note Δ is much smaller than the bulk band gap of 300 meV. This has been noted in previous measurements in similar materials (Taskin et al., 2011), and may be a result of impurity states in the bulk gap in the compensation-doped sample (while spatial variation in the doping can further reduce the observed Δ) (Skinner et al., 2013).

2.3 Hall measurements of bulk samples

Hall measurement of bulk samples with different thicknesses are performed to ensure the carriers mostly coming from the surface. See Fig. 7, the Hall resistance (R_{xy}) at low magnetic fields in three different bulk samples measured at 2 K. The linear Hall slope was used to extract the 2D carrier densities to be $6.6 \sim 7.8 \times 10^{12}\,\mathrm{cm}^{-2}$ (p type), nearly independent of thickness (varying from 20 to 52 μm), indicating surface origin of the carriers (shown in Fig. 7B). In contrast, the converted 3D carrier density n_{3D} ($= n_{2D}/t$) nearly scales as t^{-1} and is as low as $1.4 \times 10^{15}\,\mathrm{cm}^{-3}$ for the 52-μm-thick sample. Furthermore, according to the ARPES measured band structure (Arakane et al., 2012), the maximum carrier density that can be accommodated in the surface bands before occupying the bulk bands is at

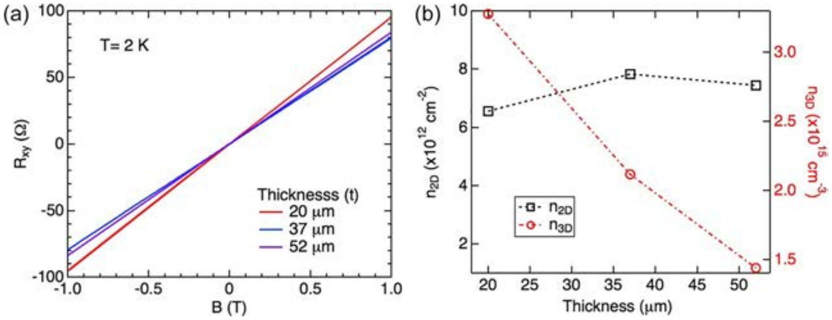

Fig. 7 (A) The Hall measurement of three bulk samples with different thicknesses. (B) The extracted 2D and 3D carrier densities from Hall measurement.

least 10^{13} cm^{-2} (both surfaces combined). Therefore, the measured Hall density comes mostly from the surface. This is also consistent with the surface-dominated conduction shown in Fig. 6 and the Fermi level residing inside the bulk band gap discussed above. Almost all the samples measured in this work (down to 20 nm thick) give densities on the order of 10^{12} cm^{-2} before gating. The true bulk density should be even lower than 1.4×10^{15} cm^{-3}, which is more than one order of magnitude lower than the lowest values from bulk-insulating 3D TIs previously reported (Analytis et al., 2010; Taskin et al., 2011; Xiong et al., 2012a).

2.4 Ambipolar field effect

Almost all the thin-flake device on Si/SiO$_2$ substrates measured have shown nice ambipolar field effect, with a single resistance peak by sweeping back-gate voltages V_{bg}, similar to that of graphene (Novoselov et al., 2005). Need to note that for samples thicker than ~100 nm, they are thick enough such that our Si/SiO$_2$ backgate can be used to independently tune the bottom surface carrier density n_b without affecting the top surface density n_t (see Fig. 8A for device schematic). Fig. 8B shows field effect measurement of a 160-nm-thick device (Sample A) at different temperatures. A single resistance peak maintains up to ~150 K, indicating high quality of samples.

The peak in R_{xx} is identified as the charge neutrality point (or Dirac point, DP) of the bottom surface, whose carriers change from electrons at higher V_{bg} to holes at lower V_{bg}. Repeated gate sweeps can have a slight hysteresis (of several volts). The ungated surfaces (both bottom surface, as seen by the field effect, and top surface) are generally found to be n-type (with electron carriers) in the exfoliated thin flakes.

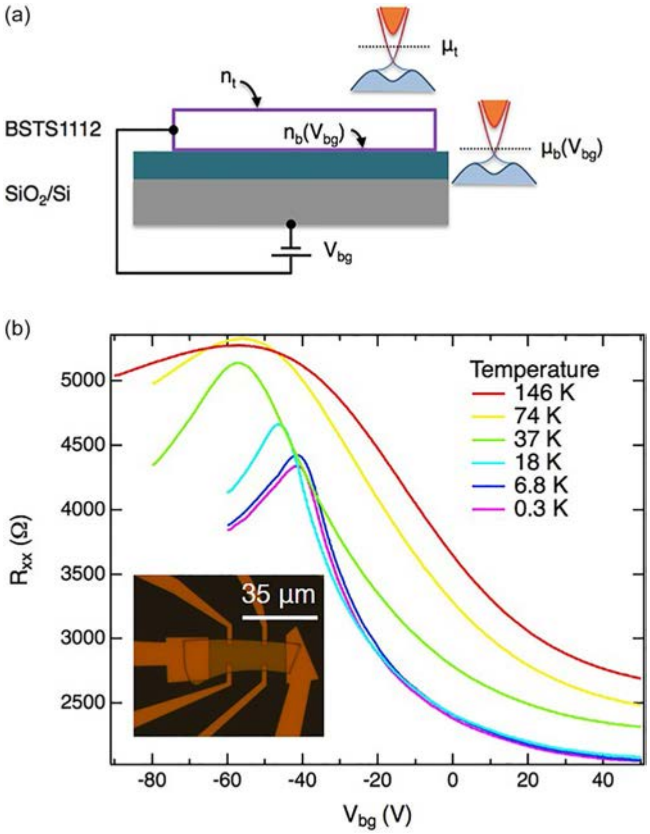

Fig. 8 (A) A device schematic, where the doped Si substrate (with 300 nm SiO_2 overlayer) is used as a backgate (V_{bg} denotes the gate voltage applied) to tune the carrier density n_b (thus the chemical potential μ_b) of the bottom surface of the BSTS. Also depicted are the Dirac surface state bands for top and bottom surfaces, respectively. (B) Field effect of Sample A measured up to ~150 K.

When both surfaces have electron carriers ($V_{bg} > -60\,\text{V}$), the $R_{xy}(B)$ shows linear behavior in low-B regime, which can be used to extract the total 2D carrier density n_{2D} and mobility μ (see Fig. 9). The linear fit of n_{2D} vs V_{bg} gives a gate efficiency of $2.7 \times 10^{10}\,\text{cm}^{-2}/\text{V}$ and the extrapolation to $V_{bg} \sim -60\,\text{V}$ (Dirac point of bottom surface) gives an approximate top surface density $\sim 0.4 \times 10^{12}\,\text{cm}^{-2}$. The highest mobility $\sim 3000\,\text{cm}^2/\text{Vs}$ is extracted when V_{bg} is close to bottom surface DP. At more negative V_{bg} ($< -60\,\text{V}$), the holes from the bottom surface will compensate for the electrons from the top surface and start to reduce R_{xy}, and $R_{xy}(B)$ start to show non-linear behavior (Fig. 9 inset).

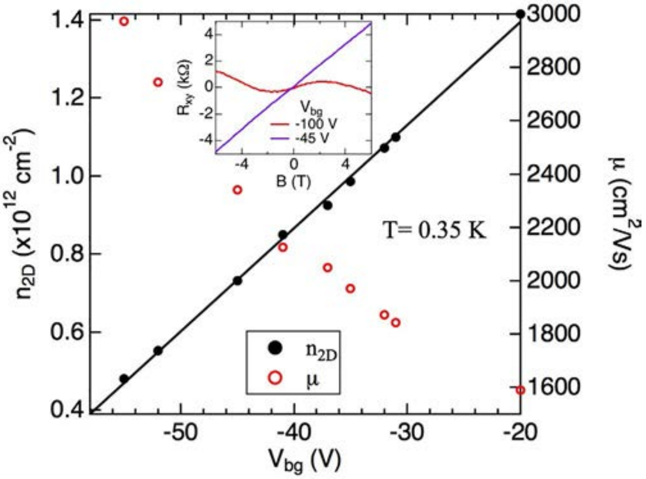

Fig. 9 Total 2D carrier density n_{2D} and mobility μ extracted from low-*B* field ($<\sim 2\,\text{T}$) transport measurements for sample A at different V_{bg}'s when both surfaces have electron carriers (n-type) such that the $R_{xy}(B)$ is linear in low-*B* regime. Inset shows R_{xy} vs *B* at $V_{bg} = -100\,\text{V}$ (electron and hole) and $-45\,\text{V}$ (both are electrons), respectively.

2.5 Weak antilocalization effect

The low-field magnetotransport measurements of our BSTS flakes show weak antilocalization (WAL) behaviors, which is a characteristic feature of a system with spin-orbit coupling. It comes from the destructive quantum interference of coherently back-scattered spin-1/2 electrons. Such a WAL can be suppressed by a magnetic field (which breaks time-reversal symmetry) and higher temperature (killing coherence), giving rise to the observed positive magnetoresistance at low temperature. The WAL in TI can be fit by the Hikami-Larkin-Nagaoka (HLN) formula (Hikami et al., 1980):

$$\Delta\sigma(B) = -\alpha \frac{e^2}{2\pi^2\hbar}\left[\ln\left(\frac{\hbar}{4el_\varphi^2 B}\right) - \Psi\left(\frac{\hbar}{4el_\varphi^2 B} + \frac{1}{2}\right)\right]$$

where $\Delta\sigma(B)$ is two-dimensional conductivity change due to magnetic field, Ψ is the digamma function, l_ϕ is the phase coherent length and α is the prefactor. For an ideal 2D TI surface which has strong spin-orbit coupling, α should be -0.5. However, in a real TI sample, two parallel surfaces (top and bottom) are involved in the conduction, giving rise to $\alpha = -1$. In BSTS flakes, α is close to -1 when both surfaces are n doped ($V_{bg} > \sim -40\,\text{V}$ in Fig. 10). When bottom surface is p doped ($V_{bg} < \sim -40\,\text{V}$) or

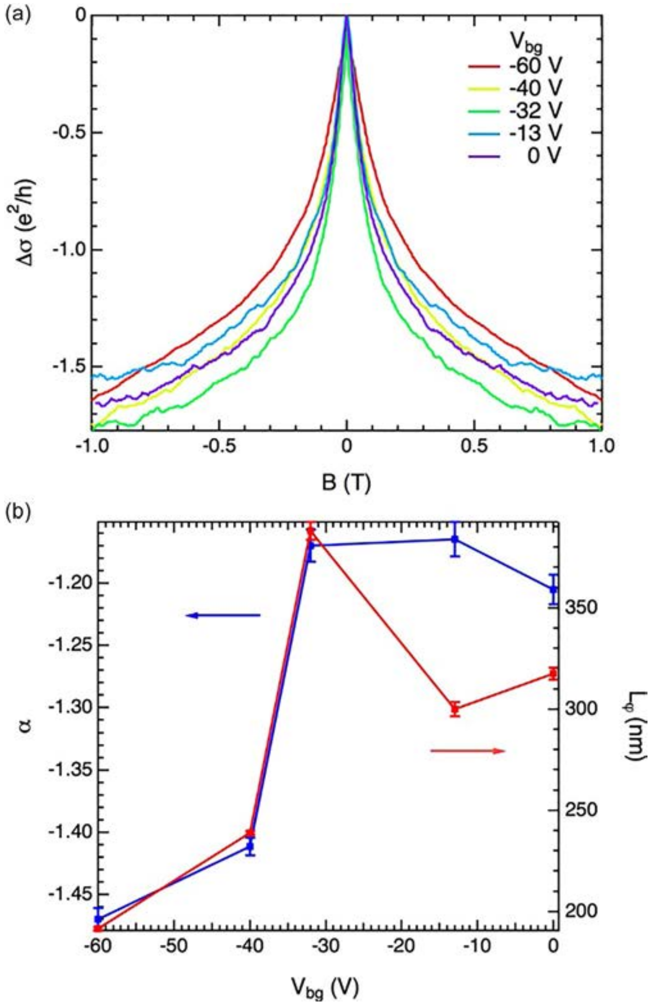

Fig. 10 (A) WAL effect in Sample A measured at different backgate voltages V_{bg}. (B) The fitting parameters α and l_ϕ as functions of the applied backgate voltage V_{bg}.

close to Dirac point ($V_{bg} \sim -40\,V$) and top surface is n doped, the fit gives α value deviates from -1. The reason is not clear so far, and it has not been reported before in this bipolar situation (Chen et al., 2010; Kim et al., 2013).

2.6 "Half-integer" quantum Hall effect in BSTS

When a back-gate tunable BSTS device (such as Sample A) is brought into a perpendicular high magnetic field B, well-developed QHE shows up.

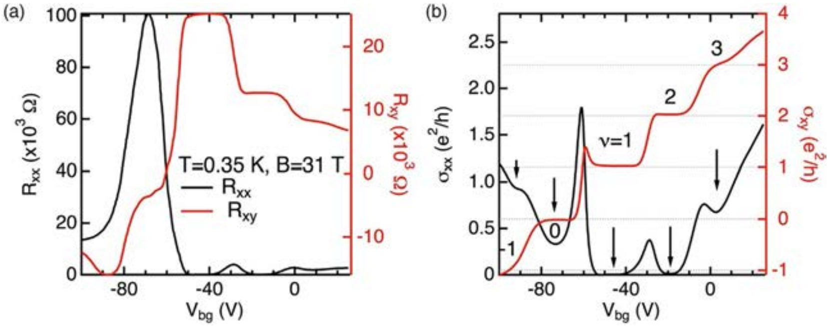

Fig. 11 (A) Longitudinal resistance (R_{xx}) and Hall resistance (R_{xy}) vs backgate voltage (V_{bg}) measured at $B=31$ T in Sample A at 0.35 K. (B) Extracted 2D longitudinal and Hall conductivities (σ_{xx} and σ_{xy}), in units of e^2/h. Plateaus observed in σ_{xy} (at $\nu e^2/h$) are labeled by the corresponding *total* Landau filling factors of the quantum Hall states. Meanwhile, arrows marked the minima or inflection in σ_{xx}.

Fig. 11A presents the longitudinal resistance R_{xx} and Hall resistance R_{xy} as functions of the backgate voltage V_{bg}, measured at $T=0.35$ K. At the electron side ($V_{bg}>-60$ V) of the bottom surface (same carrier type as the ungated top surface), we observe well-defined quantized plateaus in R_{xy} with values $\sim h/e^2 \sim 25.8\,\mathrm{k\Omega}$ and $\sim h/2e^2 \sim 12.9\,\mathrm{k\Omega}$, accompanied by vanishing R_{xx}, over broad ranges in V_{bg} around -45 and -20 V, respectively. These are the hallmarks of well-developed QHE, associated with total (top + bottom surfaces) Landau filling factors $\nu=1$ and 2, respectively (see more discussions below). In addition, a developing R_{xy} plateau $\sim h/3e^2$ is observed, accompanied by a minimum in R_{xx}. To gain more insights on the QHE, we perform tensor inversion to extract the 2D longitudinal and Hall conductivities σ_{xx} and σ_{xy}, shown in Fig. 11B in units of e^2/h. We again observe quantized (and developing) plateaus in σ_{xy} at $\nu e^2/h$ with integer $\nu=1$, 2 (and 3), concomitant with vanishing σ_{xx} (or minimum in σ_{xx}).

Such integer quantized Hall conductivities (QHC) measured can be understood as the sum of a half-integer QHC from the top surface (fixed at $e^2/2h$ at $B=31$ T) and another half-integer QHC from the bottom surface (at $\nu_b e^2/h$ with $\nu_b=1/2$, 3/2, and 5/2, etc, depending on the n_b tuned by the backgate). In other words, the observed QHC $\sigma_{xy}{}^{total}=\nu e^2/h=\sigma_{xy}{}^{top}+\sigma_{xy}{}^{bottom}=(\nu_t+\nu_b)e^2/h=(N_t+N_b+1)e^2/h$, with top (bottom) surface QHC $\sigma_{xy}{}^{top(bottom)}=\nu_{t(b)}e^2/h=(N_{t(b)}+1/2)e^2/h$, where $\nu_{t(b)}=N_{t(b)}+1/2$ and $N_{t(b)}$ are the Landau filling factor and Landau level index of top (bottom) surface corresponding to the QH state (in our case $\nu_t = 1/2$ and $N_t = 0$, thus $\sigma_{xy}{}^{top} = (1/2)e^2/h$), even though the individual (half-integer) QHC of each surface cannot be directly measured in the experiment (where we always measure the total Hall conductance of the two parallel conducting surfaces). Such a half-integer QHE reflecting the contribution in units of half quantum conductance (e^2/h) from each surface is the hallmark of the topological surface state QHE unique to 3D TI.

We further studied $\sigma_{xx}(V_{bg})$ at a series of magnetic fields (B), and found quantum Hall features can be observed down to $B = 13$ T. Fig. 12 plots σ_{xx} (color scale) as functions of both B and V_{bg}. Dashed lines trace the gate voltage (V_{bg}) positions for the observed QH minima in σ_{xx} and are labeled by the corresponding half-integer fillings (ν_b) of the bottom surface LL. When extrapolated to $B = 0$ T, these lines converge to ~-58 V, the bottom surface DP (noted as $V_D = -58$ V). Dotted lines trace the maxima in σ_{xx} labeled by corresponding integer ν_b, also extrapolate and converge to the same DP. The odd integer ratio (-3:-1:1: 3:5) in the V_{bg} positions for the QH minima in σ_{xx} as measured away from DP ($V_{bg} - $VD, proportional

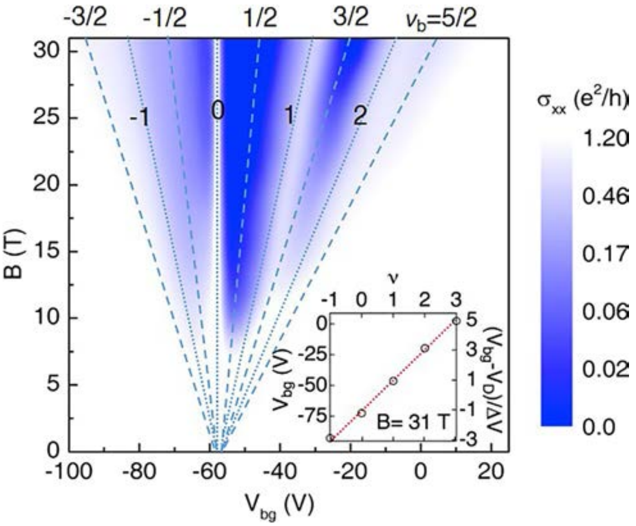

Fig. 12 A 2D color plot showing σ_{xx} (color scale) as function of B field and backgate voltage (V_{bg}) measured at 0.35 K in sample A. Dashed and dotted lines correspond to half-integer and integer Landau filling factors (marked) for the bottom surface, respectively. Inset: the V_{bg} positions for minima in σ_{xx} (left axis) and (V_{bg}-V_D)/ΔV (right axis) as a function of ν at 31 T, where ΔV is half the averaged V_{bg} separation between two consecutive Landau levels.

to n_b), exemplified in the inset for the 5 QH minima in σ_{xx} at $B=31\,T$ (corresponding to the intercepts of dashed lines on the top axis in Fig. 12), is in contrast to the QHE for conventional 2DES, where the density (filling factor) ratio for successive QHE states (σ_{xx} minima) would be consecutive integers. This half-integer shift in our data (integer/half-integer fillings for maxima/minima) is a consequence of the unique 0th LL shared half-half between Dirac electrons and holes, and a manifestation of the Berry's phase π associated with spin-helical carriers of TSS. It is known that σ_{xx} peaks when the gate tunable chemical potential (μ_b) passes through the center of last-filled LLs where the density of state (DOS) peaks and underlying state may become delocalized. The prominent central peak (the central line with $\nu_b=0$, non-dispersive with B) at DP in our σ_{xx} data represents the 0th LL, that is fixed at zero energy and non-dispersive with B, and a hallmark of Dirac fermions.

2.7 Extracting π Berry's phase for the TSS

The QHE is also measured by sweeping the magnetic field (B) at fixed carrier densities (V_{bg}). Fig. 13A upper (lower) shows R_{xy} (R_{xx}) measured vs B at $T=0.35\,K$ in sample A for various V_{bg}'s. The R_{xy}(B) trace for $V_{bg}=-52\,V$ (close to bottom surface DP) exhibits a wide quantized plateau $\sim h/e^2$ for $B>\sim 13\,T$, indicating both surfaces are in the $1/2(e^2/h)$ QH state (0th LL, $N_t=N_b=0$, $\nu=1/2+1/2=1$). When V_{bg} is increased to $-41\,V$, the higher n_b shifts the $\nu_b=1/2$ ($N_b=0$) QH state of bottom surface, thus the observed h/e^2 ($\nu=1$) plateau to higher B. Meanwhile, another QH plateau develops at $h/2e^2$ at lower $B\sim 15\,T$ (but still $>\sim 13\,T$ with $N_t=0$), corresponding to $N_b=1$, $\nu=\nu_t+\nu_b=1/2+3/2=2$. This QH state also shifts to higher B as V_{bg} increases (-35, -30 and $-20\,V$). Further increasing V_{bg} to -14, -5 and $2\,V$, yet another QH plateau develops at $h/3e^2$, now corresponding to $N_t=0$, $N_b=2$, $\nu=\nu_t+\nu_b=1/2+5/2=3$. All these QH plateaus are accompanied by vanishing R_{xx} or dips in R_{xx}, with each QH state generally better developed at higher B (reflecting the larger LL energy gap).

From the evolution of the QH states seen in Fig. 13A for $B>\sim 13\,T$, we can extract the bottom surface LL index N_b (note N_t is fixed at 0) and perform the standard fan diagram analysis (Fig. 13B, showing N_b vs $1/B$), where integer/half- integer N_b is assigned the minima/maxima in R_{xx} (or alternatively in dR_{xy}/dB, with an example shown in Fig. 13B inset). We find N_b vs $1/B$ (exhibiting good linear fit) extrapolates (in the limit

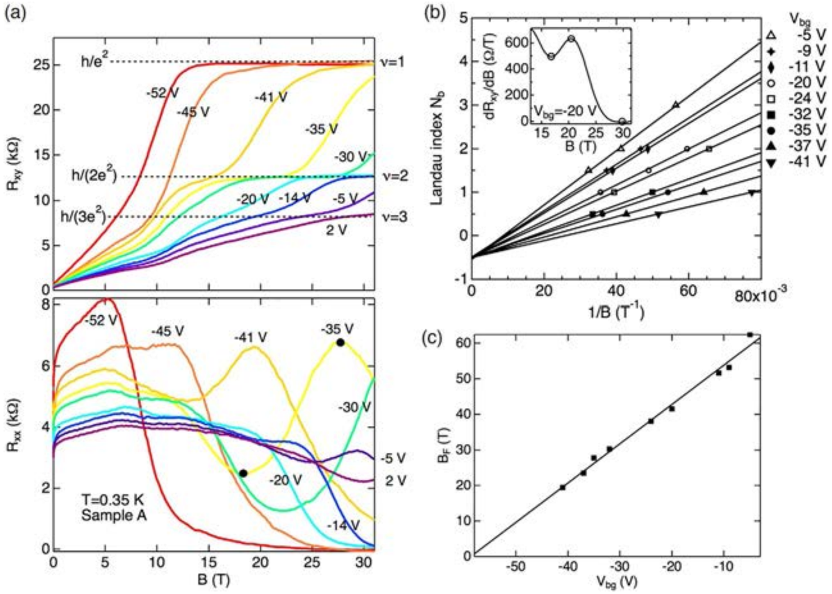

Fig. 13 (A) R_{xy} and R_{xx} as functions of B at various V_{bg}'s. Several observed quantum Hall plateaus are marked with corresponding total Landau filling factors ν. (B) Landau fan diagram for the bottom surface for various different V_{bg}'s. Data in solid markers are extracted from R_{xx}(B) while those in empty markers from the derivative of R_{xy}(B) (an example at $V_{bg} = -20$ V is shown in the inset). Examples of extracted data points are marked in the inset and R_{xx} trace for $V_{bg} = -35$ V. Only data with $B > \sim 13$ T (where the top surface is at its 0th LL) are used. Lines denote linear fits with N_b-axis intercept $\sim -1/2$ for all datasets. (C) SdH oscillation frequency B_F of bottom surface extracted from (B) as a function of V_{bg}.

of $1/B \rightarrow 0$) to an N-axis intercept of $\sim -1/2$ for all V_{bg}'s studied. Such a 1/2-intercept in LL index is again a hallmark of π Berry's phase for Dirac fermions and underlies the half-integer QHE.

As the bottom surface density can be extracted as $n_b = eB_F/h$ (where B_F is the SdH oscillation frequency), the gate efficiency can be extracted from the linear fit of B_F vs V_{bg} to be $2.7 \times 10^{10}\,\mathrm{cm}^{-2}/\mathrm{V}$ (Fig. 13C), consistent with the result in Fig. 9. The matching of density extracted from QH and low-field Hall data also indicates that the carriers contributing to the transport is completely from the TSS in our BSTS. There are no other parallel conducting channels in our BSTS. However, the value $2.7 \times 10^{10}\,\mathrm{cm}^{-2}/\mathrm{V}$ is notably smaller than $7.3 \times 10^{10}\,\mathrm{cm}^{-2}/\mathrm{V}$ given by the simple capacitance of 300-nm thick SiO_2, possibly due to trapped charged impurities in the oxide or other screening effects. The extrapolated linear fit to $V_{bg} = \sim -60$ V gives B_F close to zero, consistent with expected vanishing carrier density of bottom surface near its DP.

2.8 Temperature dependence of the QHE

Fig. 14 shows backgate-tuned QHE (R_{xx} and R_{xy} vs V_{bg}) measured a fixed $B = 31$ T in another BSTS device Sample B (thickness $t = 80$ nm) at different temperatures (T). At low T (4.5 K), we observe QH states corresponding to $\nu = 1$ (well-developed) and $\nu = 2$ (developing), interpreted (similarly to Sample A, Fig. 11) to $\nu_{\mathrm{t}} + \nu_{\mathrm{b}} = 1/2 + 1/2$ and $1/2 + 3/2$, respectively. The insensitivity of the quantization values to the sample thickness (changing by factor of 2 between samples A and B) confirm that the observed QHE arises from the surface of the intrinsic TI, and is not related to the "bulk" QHE observed previously (in highly-bulk-doped Bi_2Se_3, attributed to electronic decoupling between bulk quintuple layers with high Se vacancies) (Cao et al., 2012). As seen in Fig. 14A, increasing T does not weaken substantially the QH states till at least ~10 K, and QH states are still observable up to 35 K, before disappearing above ~50 K. Fig. 14B and C show more quantitative analysis of the T dependence of the QHE at $\nu = 1$ (both surface

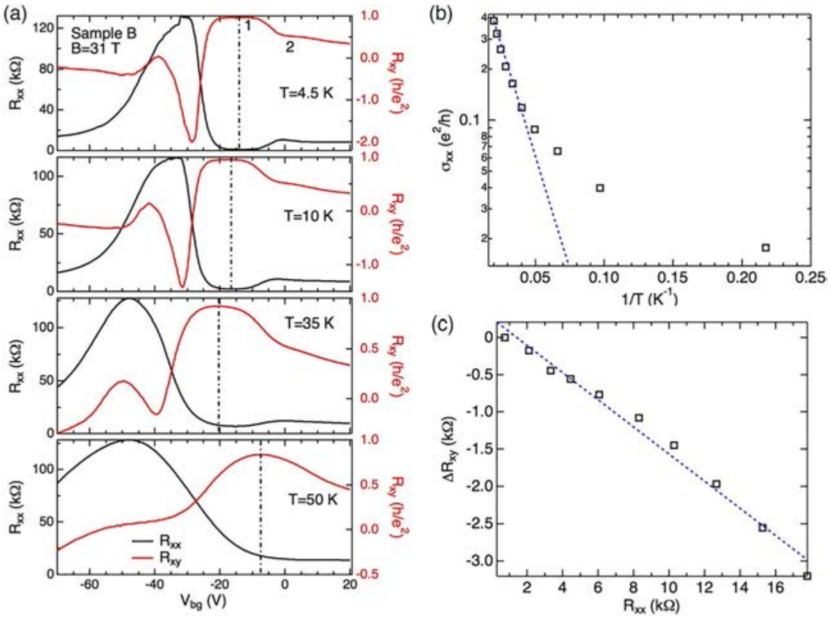

Fig. 14 Measurements were performed in Sample B, an 80-nm-thick exfoliated BSTS flake. (A) V_{bg} dependent R_{xx} and R_{xy} measured at $B = 31$ T and 4 different temperatures (0.35, 10, 35, and 50 K). Vertical dot-dashed lines indicate the position of QH state at total filling factor $\nu = 1$ (the shifts in V_{bg} positions may reflect thermally induced carrier density change). (B) σ_{xx} (log scale) as function of inverse temperature (1/T) at $\nu = 1$. Blue dashed line indicates a fit in higher temperature with $\sigma_{xx} \propto \exp(-E_0/kT)$. (c) ΔR_{xy} vs R_{xx} at $\nu = 1$. Blue dashed line indicates a linear fit.

filling 0th LL). The σ_{xx} (QH minimum) exhibits a thermally activated behavior ($\propto e^{-E_0/k_B T}$) at higher T (Fig. 14B) with an extracted activation gap $E_0 \sim 5.6 \pm 0.3\,\text{meV}$, but drops more slowly with decreasing T at lower T. The E_0 value is notably smaller than the theoretical energy separation $v_F(2eB\hbar)^{1/2}$ ~60 meV between the 0th and 1st LLs of ideal 2D Dirac fermions, for a typical Fermi velocity $v_F \sim 3 \times 10^5\,\text{m/s}$ estimated from ARPES measurements. This could stem from both disorder-induced Landau level broadening (such an effect was also seen in graphene with similar mobility) (Jabakhanji et al., 2014) and a finite thickness (side surface) effect. At even higher temperature (>50 K), the bulk conduction starts to become significant and possibly suppress the QH states. The thermally induced change ΔR_{xy} ($=R_{xy}(T) - R_{xy}(4.5\,\text{K})$) vs R_{xx} at $\nu = 1$ follows an approximately linear relationship (with a slope of −0.18, Fig. 14C). The T dependence behaviors of the QHE observed in our BSTS are quantitatively similar to those of the previously studied integer QHE in 2DEG.

2.9 Discussion

Well-developed "half-integer" QHE was previously observed for Dirac fermions (fourfold degenerate with 2 spins and 2 valleys) in graphene (Novoselov et al., 2005; Zhang et al., 2005), giving QHC $\sigma_{xy} = 4(N + 1/2)e^2/h$. A zero-gap HgTe quantum well was found to give a 2DES with single-valley Dirac fermions (thus considered "1/2-graphene," with two spins), and exhibit well-defined QHE (Büttner et al., 2011). In contrast, a TI surface contains only 1 species of Dirac fermions (a single non-degenerate Dirac cone, sometimes referred to a "1/4- graphene"), resulting in a QHC of $(N+1/2)e^2/h$. Two such degenerate surfaces contribute in parallel to give the observed $\sigma_{xy} = 2(N+1/2)e^2/h$ (odd integer plateaus). The surface (top or bottom) index in our sample can be viewed as a pseudospin, which is not affected by external B field. One can use a gate voltage (controlling the chemical potential difference between two surfaces, thus acting as a fictitious Zeeman field) to make the pseudospins degenerate (giving odd integers of QHC, Fig. 13) or non-degenerate (giving consecutive integers of QHC, Fig. 11), realizing a more tunable system. However, a complete understanding of some of the QH states (such as in the bipolar situation) and underlying mechanism would favor an independent gating of the densities and carrier types of both top and bottom surfaces. Further work on dual-gated BSTS devices would be presented in the next few sections.

3. Quantum transport in dual-gated 3D topological insulators

3.1 Dual-gated device fabrication

Similarly, as discussed in the last section, BSTS flakes (typical thickness ~50–200 nm) are exfoliated (Scotch tape method) onto highly doped Si (p+) substrates (with 300 nm-thick SiO2 coating), and deposited with Cr/Au contacts after e-beam lithography. The BSTS flakes are then etched into standard Hall-bar geometry by Argon plasma (dry etching) to eliminate uncertainties in evaluating conductivities due to the influence of electrical contacts or the irregular shape of the samples. A thin flake of hexagonal boron nitride (h-BN, typical thickness ~10–40 nm) is mechanically transferred on the BSTS flake to serve as a top-gate dielectric and a top-gate metal (Cr/Au) is deposited afterwards. The h-BN as a substrate or gate dielectric is known to preserve good electronic properties for graphene, resulting from the atomic flatness and relatively low density of impurities in h-BN (Dean et al., 2010). Temperature above 130°C is avoided during the fabrication process to prevent any heating induced doping effect. See Fig. 15 for a schematic of a dual-gated BSTS device and the fabrication procedures.

3.2 Independent gating of top and bottom surfaces

Qualitatively similar data are measured in multiple samples, while results from a typical sample C (channel length $L=9.4\,\mu\mathrm{m}$, width $W=4.0\,\mu\mathrm{m}$, with ~100 nm- thick BSTS and 40 nm-thick h-BN as top-gate dielectric) are presented below unless otherwise noted. The carrier densities of the

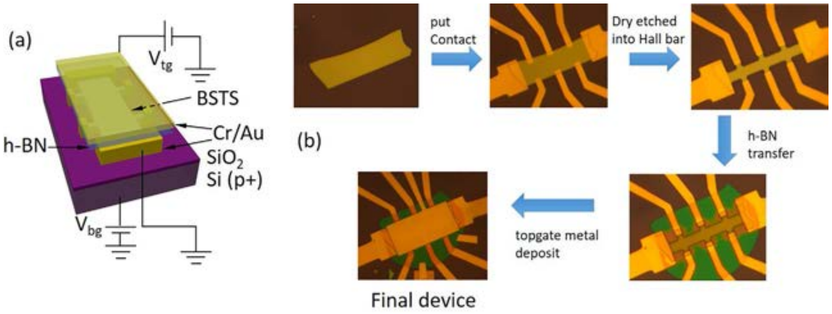

Fig. 15 (A) A dual-gated BSTS device schematic. (B) Optical images and device fabrication procedure for a typical dual-gated device Sample C.

top and bottom surface of the BSTS flake are tuned by top-gate voltage V_{tg} (applied to top-gate metal) and back-gate voltage V_{bg} (applied to Si substrate), respectively. Fig. 16A and B show the double-gated electric field effect measured at $T = 0.3\,K$. The longitudinal resistivity ρ_{xx} at magnetic field $B = 0\,T$ (Fig. 16A) and Hall resistivity ρ_{xy} at $B = 1\,T$ (Fig. 16B) are plotted in color scale as functions of both top and bottom gate voltages (V_{tg} and V_{bg}).

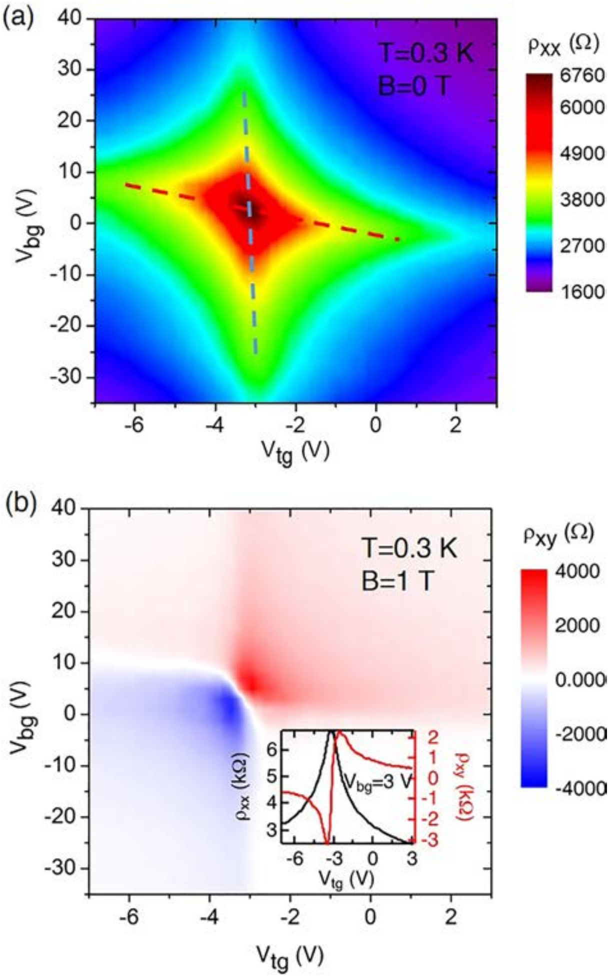

Fig. 16 (A) and (B) show 2D map of ρ_{xx} at $B = 0\,T$ and ρ_{xy} at $B = 1\,T$ as functions of V_{tg} and V_{bg} on sample C. The blue (red) dashed lines in (A) are guides to the eye for the top (bottom) surface DP. The 2D map is generated by data measured from V_{tg} sweeps at a series of V_{bg}'s, with one example at $V_{bg} = 3\,V$ shown in the inset of (B).

The extracted field effect and Hall mobilities are typically several thousands of $\mathrm{cm^2/Vs}$. A minimum carrier density $n^* \sim 9\times10^{10}\,\mathrm{cm^{-2}}$ per surface can be extracted from the maximum Hall coefficient (absolute value) $\sim 3.5\,\mathrm{k\Omega/T}$ (when both surfaces are slightly n-type or p-type) measured in Fig. 16B. A set of exemplary V_{tg}-sweeps with $V_{\mathrm{bg}}=3\,\mathrm{V}$ is shown in Fig. 16B inset. By adjusting V_{tg} (or V_{bg}), the device can be gated through a ρ_{xx} peak, identified as the charge neutrality Dirac point (DP) of the top (or bottom) surface, marked by the blue (or red) dashed lines in Fig. 16A. Gating through the DP, the carriers in the corresponding surface change from hole-like to electron-like (i.e., ambipolar), as evidenced by Hall measurements (Fig. 16B). The slight deviation of the two lines from being perfectly vertical and horizontal arises from the weak capacitive coupling between the top (bottom) surface and the back (top) gate (Fatemi et al., 2014). The crossing of these two lines corresponds to the double-DP (both surfaces tuned to DP) where ρ_{xx} ($\sigma_{\mathrm{xx}}=1/\rho_{\mathrm{xx}}$) reaches a global maximum (minimum). Within the gate voltage range used, the carriers predominantly come from the TSS and we observe relatively good particle-hole symmetry in the transport properties (e.g., the symmetrical appearance of ρ_{xx} on both sides of DP in each surface in Fig. 16A and the similar absolute values of the positive and negative maximum Hall coefficient in Fig. 16B).

3.3 Gate efficiency and mobility of each surface

Now we present how to extract the gate efficiency and mobility for each surface of Device C (inter-surface capacitance coupling is neglected here). From the color map of ρ_{xx} and ρ_{xy}, we identify the double Dirac point (at which both surfaces are tuned to Dirac point) located at (V_{tg}, V_{bg}) $\sim$ ($-3.13\,\mathrm{V}$, $2.5\,\mathrm{V}$). We performed line cuts for the longitudinal conductivity σ_{xx} ($=1/\rho_{\mathrm{xx}}$ at $B=0$) and calculated density n ($=1/e\rho_{\mathrm{xy}}=1/eR_{\mathrm{xy}}$ at $B=1\,\mathrm{T}$) color maps at fixed $V_{\mathrm{bg}}=2.5\,\mathrm{V}$ or $V_{\mathrm{tg}}=-3.13\,\mathrm{V}$ (shown in Fig. 17). The gate efficiency for top and backgates are extracted to be 1.7×10^{11} and $2.9\times10^{10}\,\mathrm{cm^{-2}/V}$, respectively, from the linear fitting of n vs the corresponding gate voltage on the electron doped side (some nonlinearity presents in the negative doping side due to the existence of both charge carrier types). The mobility for each surface can be extracted through Drude model $\mu=\frac{1}{e}\frac{d\sigma_{xx}}{dn}=\frac{1}{e}\frac{d\sigma_{xx}}{dV}/\frac{dn}{dV}$, where we use $\frac{d\sigma_{xx}}{dV}$ obtained from the linear fitting near the Dirac point in Fig. 17A and C. The mobility for the top and bottom surfaces are then calculated to be of comparable values $\sim$2500 and $\sim 2000\,\mathrm{cm^2/Vs}$, respectively.

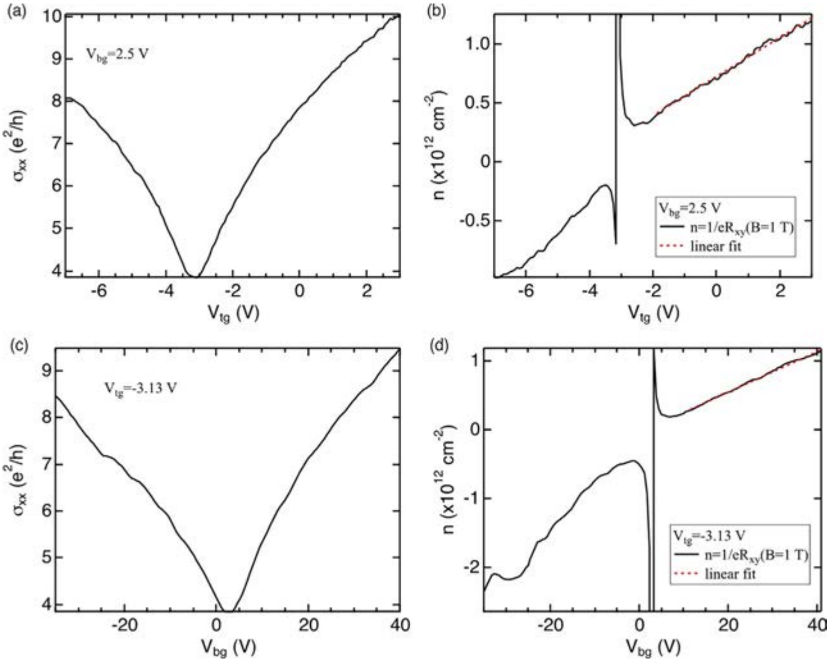

Fig. 17 (A and B) The line cuts of σ_{xx} (A) and *n* (B) as a function of V_{tg} at $V_{bg}=2.5$ V. (C and D) The line cuts of σ_{xx} (A) and *n* (B) as a function of V_{bg} at $V_{tg}=3.13$ V. In (B) and (D), we also show the linear fittings (dashed red lines) for the density *n* vs gate voltage to extract gate efficiency on the electron doped side.

3.4 Minimum conductivity at double Dirac point

We have studied six dual-gated BSTS devices with different thicknesses (t) and aspect ratios (L/W). These devices are measured at low temperatures ($T<2$ K) and the results are repeatable after multiple thermal cycles. When both surfaces are tuned to DP, the minimum 2D conductivity $\sigma_{\min}$ at $B=0$ T exhibits relatively constant value $(3.8\pm0.1)e^2/h$ for all the devices measured (with the uncertainty representing 90% confidence interval), whose thicknesses range from 50 to 195 nm and L/W range from 1.3 to 3.5 (Fig. 18). Our observation indicates that the conductivity at the DP for each major surface (top or bottom) is $\sim 2e^2/h$, within the range of values (2–5 e^2/h) reported by Kim et al. (2012a) on thin flakes of Bi_2Se_3 ($\sim$10 nm). The better consistency over multiple samples in our dual-gated BSTS devices may be attributed to the more insulating bulk (whose conduction is immeasurably small at low temperature) and uniformity of the exfoliated BSTS flakes, which are sandwiched between SiO_2 and h-BN to achieve

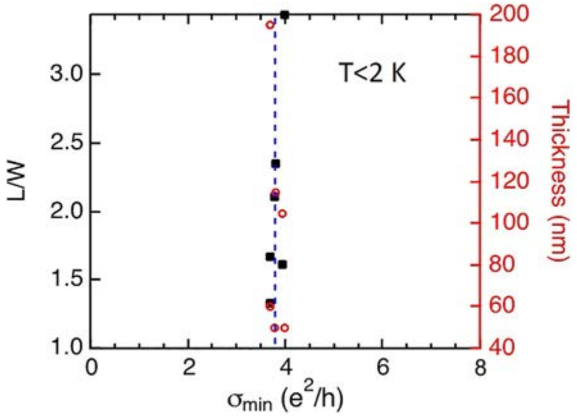

Fig. 18 Zero-magnetic-field minimum conductivity σ_{min} (bottom axis) measured in six dual-gated samples at low temperature ($<2K$) plotted as a function of the sample thickness and 2D aspect ratio (L/W). The vertical dashed line indicates $3.8e^2/h$.

better device stability. The minimum conductivity at DP has also been discussed in graphene with considerable interest (Chen et al., 2008; Das Sarma et al., 2011; Martin et al., 2008; Miao et al., 2007; Nilsson et al., 2006; Tan et al., 2007).

For pristine graphene, a minimum conductivity min of $4e^2/\pi h$ is predicted and experimentally verified in ballistic graphene samples (Das Sarma et al., 2011; Miao et al., 2007). For graphene samples with more scattering, σ_{min} was reported to have a universal value of $4e^2/h$ (Novoselov et al., 2005) while another experiment observed σ_{min} that falls into a wide range 2–$12e^2/h$ varying from sample to sample (Tan et al., 2007). Further experiments revealed that the minimum conductivity is strongly affected by carrier density inhomogeneities (puddles) induced by disorder on or near graphene (Chen et al., 2008; Martin et al., 2008), such as the absorbates or charged impurities in the substrates. In 3D TIs, one source of impurities likely relevant to the observed quasi-universal minimum conductivity in our dual-gated BSTS devices could be bulk defects (located near surface) (Skinner et al., 2013), such as those revealed in scanning tunneling microscopy studies (Beidenkopf et al., 2011).

3.5 Dual-gate tunable QHE

Now we start to focus on the transport phenomena in the quantum Hall (QH) regime under a high magnetic field B perpendicular to the top and bottom surfaces in the dual-gated Sample C. Fig. 19 show in color scales

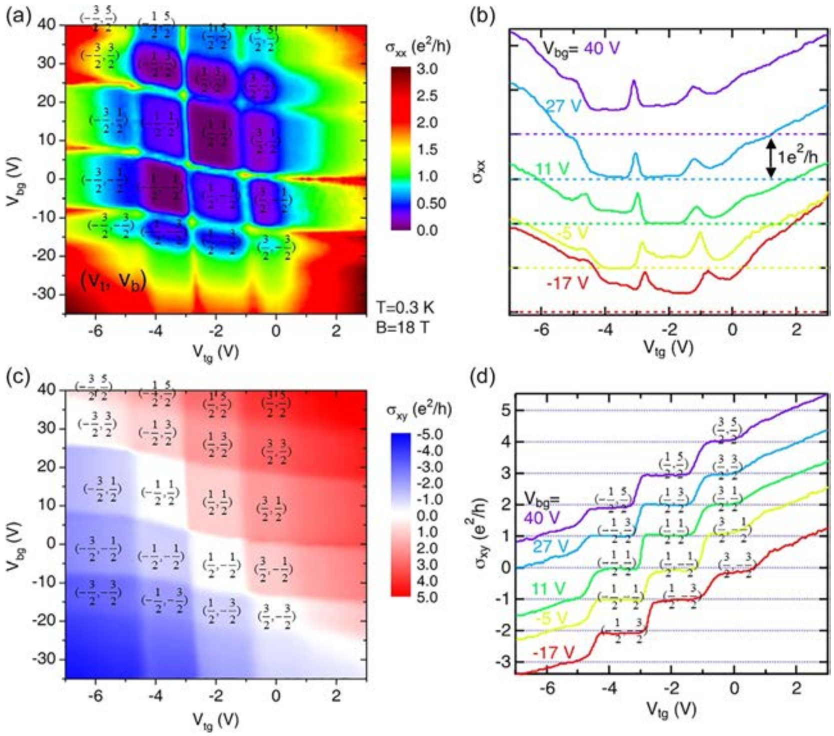

Fig. 19 (A) σ_{xx} and (C) σ_{xy}, shown as 2D color maps, as functions of V_{tg} and V_{bg} at $B = 18$ T and $T = 0.3$ K in Sample C, with representative cuts at five different V_{bg}'s shown in (B) and (D). The (ν_t, ν_b) labels (top, bottom) surface filling factors for corresponding quantum Hall states. The σ_{xx} curves in (B) are shifted vertically (in consecutive step of e^2/h) for clarity (the corresponding zero σ_{xx} levels are indicated by the same-colored horizontal dashed lines).

the longitudinal conductivity σ_{xx} and Hall conductivity σ_{xy} as functions of V_{tg} and V_{bg} at $B = 18$ T and $T = 0.3$ K. The color plots in Fig. 19A and C divide the (V_{tg}, V_{bg}) plane into a series of approximate parallelograms, centered around well-developed or developing QH states with vanishing or minimal σ_{xx} (Fig. 19B) and quantized σ_{xy} in integer units of e^2/h (Fig. 19D). These QH parallelograms are bounded by approximately (but slightly tilted) vertical and horizontal lines, which represent the top and bottom surface LLs, respectively. By increasing (decreasing) either V_{tg} or V_{bg} to fill (exhaust) one LL on the top or bottom surface, σ_{xy} increases (decreases) by e^2/h, taking consecutive quantized values of $\nu e^2/h$, where integer $\nu = \nu_t + \nu_b = N_t + N_b + 1$. The $N_{t(b)}$ is the corresponding top (bottom) surface LL integer index that can be adjusted by top (back) gate to be of either

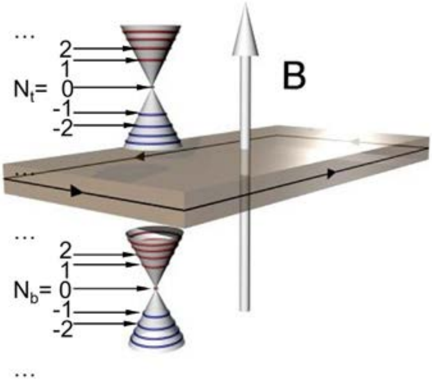

Fig. 20 A schematic of the LLs developed on the top and bottom surfaces of a slab-like 3D TI sample with applying a perpendicular magnetic field, where $N_{t(b)}$ labels the corresponding LL index for the top (bottom) surface.

Dirac electrons or holes (see a schematic in Fig. 20). In Fig. 19D, different fixed V_{bg}'s (from −17 to 40 V) set ν_b around consecutive half integers −3/2, −1/2, 1/2, 3/2 and 5/2 (such that the bottom surface contributes $\sigma_b = \nu_b{}^* e^2/h$ to the total σ_{xy}), explaining the vertical shift of e^2/h at QH plateaux of consecutive V_{tg} sweeps.

It is also notable that in Fig. 19, there are a few states with zero quantized Hall conductivity ($\sigma_{xy} = 0$, manifesting as white regions in Fig. 19C, separating the electron-dominated regions in red and the hole-dominated regions in blue) and non-zero σ_{xx} minimum, marked by equal and opposite half-integer values of ν_t and ν_b thus total $\nu = 0$, for example (ν_t, ν_b) = (−1/2, 1/2), (1/2, −1/2) and (3/2, −3/2). These states with total $\nu = 0$, exhibiting zero Hall plateaux (see also Fig. 19D), have non-zero σ_{xx} minimum (Fig. 19A) but very large R_{xx} maximum (see Section 3.6, Fig. 21).

3.6 Non-local measurements

To further characterize the observed QH and $\nu = 0$ states, we have performed nonlocal transport measurements of R_{nl} (= V_{nl}/I, I is the current and V_{nl} is the non-local voltage, see the schematic measurement setup in the inset of Fig. 21B) as functions of V_{tg} and V_{bg} at $B = 18$ T and $T = 0.3$ K and compared the results with the standard (local) measurements of the longitudinal resistance R_{xx} (Fig. 21A). It's intriguing that unlike other QH states typified by a zero or minimum in R_{xx}, the states with $\nu = \nu_t + \nu_b = 0$ (labeled by (ν_t, ν_b) in Fig. 21A with $\nu_t = -\nu_b = 1/2$ or 3/2) are accompanied by a R_{xx} maximum. The best-developed $\nu = 0$ states are

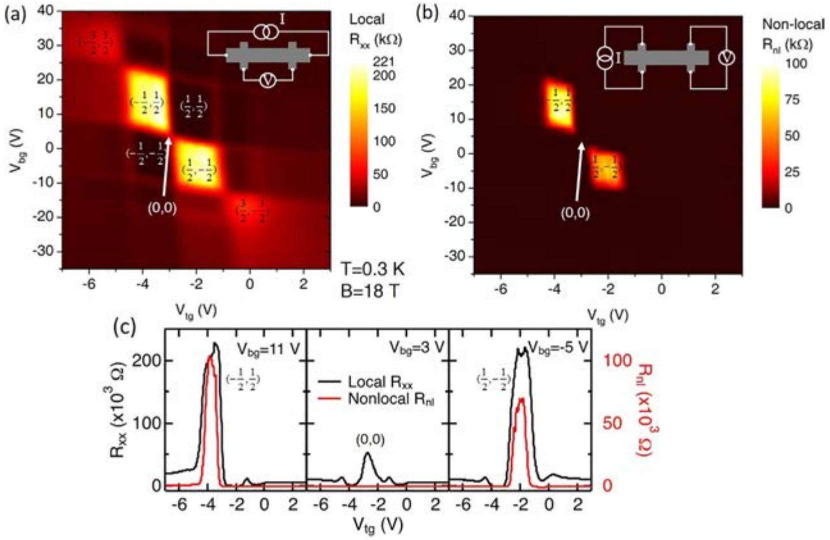

Fig. 21 (A) Local resistance R_{xx} and (B) non-local resistance R_{nl} measured in Sample C as functions of V_{tg} and V_{bg} at $B=18$ T and $T=0.3$ K, with insets showing the measurement setup schematics. (C) A few representative cuts of (A) and (B) at different V_{bg}'s.

those at $(\nu_t, \nu_b)=(-1/2, 1/2)$ or $(1/2, -1/2)$, where R_{xx} reaches 220 kΩ ($\rho_{xx}\sim 100$ kΩ), exceeding the resistance quantum ($h/e^2=\sim 25.8$ kΩ) by an order of magnitude. The nonlocal R_{nl} also becomes very large (~100 kΩ) and the similar order of magnitude as R_{xx} at these two $\nu=0$ states while negligibly small at other (ν_t, ν_b) states (see Fig. 21B and also the representative cuts in Fig. 21C).

The simultaneously large local and non-local resistance at $\nu=0$ states in the QH regime has been reported in other 2D electron-hole systems (Gusev et al., 2012; Nichele et al., 2014) and understood in a picture of dissipative edge channels. We emphasize that the pronounced R_{nl} signal cannot be explained from R_{xx} by a classical Ohmic non-local resistance from the stray current connecting the remote leads. Such a contribution ($=\sim\rho_{xx}e^{-\pi L/W}$) would decay exponentially with L/W (=2.4 in our case), and be three orders magnitude smaller than the local R_{xx} (which is the case at $B=0$ T, Fig. 22). As another comparison, the middle panel of Fig. 21C shows the cuts in Fig. 21A and B at $V_{bg}=3$ V, crossing the double-DP (also zeroth LL) of both top and bottom surfaces at $(\nu_t, \nu_b)=(0,0)$, where we observe a relatively large peak in R_{xx} but significantly smaller R_{nl}. Such a result is consistent with the *extended* state transport (at the center of zeroth LL) as the current flows through the bulk of the 2D surface.

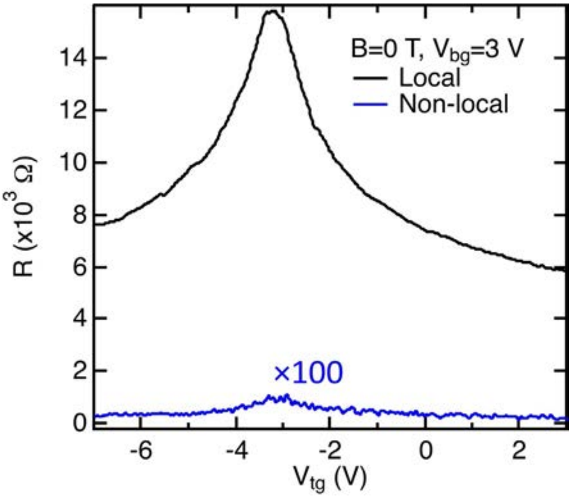

Fig. 22 Local resistance R_{xx} (A) and non-local resistance R_{nl} (B) as functions of V_{tg} at $V_{bg}=3$V and $B=0$T, $T=0.3$K. The non-local resistance R_{nl} shown here is multiplied by a factor of hundred.

From the color plots in Figs. 19 and 21, the parallelogram centered around $(\nu_t, \nu_b)=(-1/2, 1/2)$ state is enclosed by boundaries representing $N_t=0$ and -1, $N_b=0$ and 1 LLs. Similarly, $(\nu_t, \nu_b)=(1/2, -1/2)$ state is bounded by $N_t=0$ and 1, $N_b=0$ and -1 LLs. We conclude that such a $\nu=0$ state can exist when the potential difference V between top and bottom surfaces (equivalently the energy separation between top and bottom surface DPs) is in the range of $0<|V|<2E_{0-1}$ ($\approx 2\times 50$meV at $B=18$T, where E_{0-1} is the 0–1 LL separation of TSS Dirac fermions (Xu et al., 2014)). The large energy scale of E_{0-1} can help make the $\nu=0$ and $\nu=\pm 1$ QH states observable at significantly elevated temperatures as demonstrated below.

3.7 Temperature dependence study

We have studied the temperature (T) dependence of the QHE and $\nu=0$ states from 0.3 to 50K at $B=18$T (Fig. 23). At each temperature, the bottom surface density is tuned by V_{bg} to set ν_b near 1/2 (dashed lines) or $-1/2$ (solid lines), and the peaks in local R_{xx} and nonlocal R_{nl} corresponds to $(\nu_t, \nu_b)=(-1/2, 1/2)$ or $(1/2, -1/2)$, respectively. The R_{xx} peaks ($>\sim 150$ kΩ) are seen to be more robust up to the highest temperature ($T=50$K) measured while R_{nl} peaks decrease rapidly (approximately linearly in T, shown in the inset of Fig. 23B) with increasing T and is nearly suppressed above 50K.

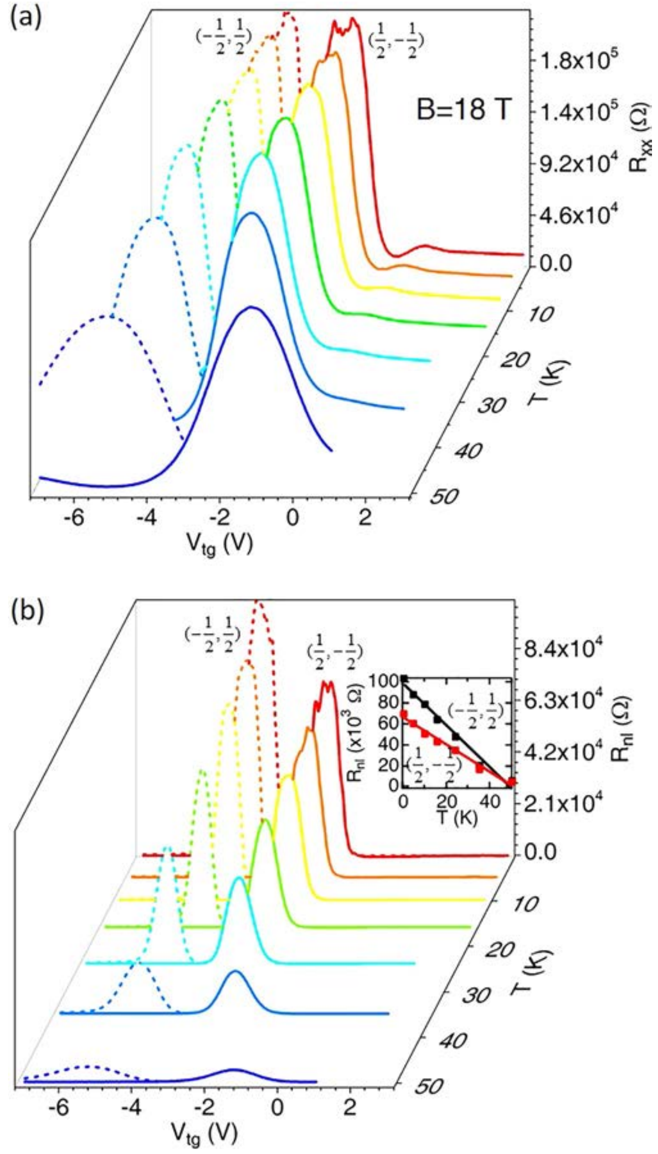

Fig. 23 (A) R_{xx} and (B) R_{nl} measured in sample C as functions of V_{tg} for different temperatures at $B = 18$ T, where V_{bg} is chosen to set ν_b at 1/2 (dashed lines) and $-1/2$ (solid lines), respectively. The inset of (B) shows approximately linear dependence of R_{nl} peaks at $\nu = 0$ on temperature.

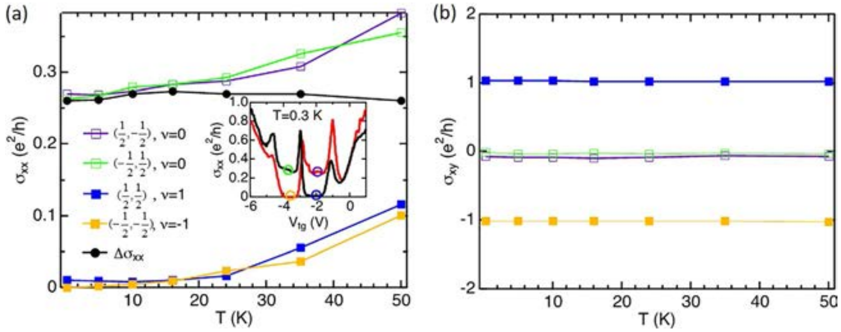

Fig. 24 (A) σ_{xx} and (B) σ_{xx} of $\nu = +1$, -1 and 0 states as functions of temperature. In (C), we also plot σ_{xx} (difference between averaged $\nu = 0$ σ_{xx} and averaged $\nu = \pm 1$ σ_{xx}), which barely changes with T.

We also show the T-dependence of σ_{xx} and σ_{xy} at $(\nu_{\mathrm{t}}, \nu_{\mathrm{b}}) = (-1/2, 1/2)$, $(1/2, -1/2)$, $(1/2, 1/2)$ and $(-1/2, -1/2)$ in Fig. 24A and B. The σ_{xy} maintains good quantization at $\nu e^2/h$ ($\nu = 0, \pm 1$) up to $T = 50\,\mathrm{K}$ while σ_{xx} increases with T. The σ_{xx} for $\nu = \pm 1$ states is found to show thermally activated behavior at high temperatures (Xu et al., 2014), where the finite σ_{xx} is attributed to the thermal excited 2D surface or 3D bulk carriers. Such carriers can shunt the edge-state transport and suppress the nonlocal R_{nl} response at high T (Gusev et al., 2012). We also note that the σ_{xx} vs T curves for $\nu = 0$ and $\nu = \pm 1$ states follow the similar trend and have approximately constant separation. We find the averaged separation $\Delta\sigma_{\mathrm{xx}} = 1/2^*[\sigma_{\mathrm{xx}}(-1/2,1/2) + \sigma_{\mathrm{xx}}(1/2,\text{-}1/2)\text{-}\sigma_{\mathrm{xx}}(1/2,1/2)\text{-}\sigma_{\mathrm{xx}}(-1/2,\text{-}1/2)]$ to be largely T-independent with a value of $(0.27 \pm 0.01)e^2/h$, which we attribute to the conductivity of the quasi-1D dissipative edge channel.

3.8 Dissipationless and dissipative edge states

In this section, I would describe how to understand the QHE in 3D TIs and discuss some remaining open questions.

The surface of a slab-like 3D TI has a closed 2D manifold and the topology of a sphere, thus geometrically different from conventional 2D electron gases with a planar structure (Lee, 2009). The QHE, arising from LL confinement near the edges, is not obvious how it works and whether it exists in a 3D TI (we consider the bulk to be totally insulating/empty here for simplicity) (Lee, 2009; Vafek, 2011; Zhang et al., 2012). In such slab-like 3D TI samples under perpendicular magnetic field, the side surface only experiences an in-plane field that has no orbital effect while top and bottom surfaces experience magnetic flux along and opposite to the surface normal, respectively. Of course, in the thick limit (sample thickness $t \gg l_B$, where $l_B = \sqrt{\hbar/eB}$ is the magnetic length), the energy spectrum on side surfaces would approach the normal Dirac-like continuum for TSS (Vafek, 2011). In this case, the delocalized states on side surfaces would inevitably short opposite edges (namely side surfaces) and spoil the QHE in a normal Hall-bar structure (Lee, 2009; Vafek, 2011). A "Corbino" structure is proposed to be able to give QHE in this scenario (Lee, 2009).

In the thin sample limit ($t \ll l_B$, without considering any top and bottom surface hybridization effect here), the side surfaces can be viewed as a quai-1D domain boundary that separates the top and bottom surfaces with B pointing outward and inward, respectively, thus can support dissipationless QH edge states (Chu et al., 2011). In this case, when the top and bottom surfaces are doped to the same carrier type (either n or p), the corresponding QH edge states (on the side surface) would have the same chirality and give the total $\sigma_{\mathrm{xy}} = \nu e^2/h = (\nu_{\mathrm{t}} + \nu_{\mathrm{b}})e^2/h$, restricted to integer multiples of e^2/h. Meanwhile the longitudinal resistivity (ρ_{xx}) or conductivity (σ_{xx}) vanishes because of the ballistic edge states.

When the sample thickness is in the intermediate regime ($t \sim l_{\mathrm{B}}$), it's not clear whether the well-defined QHE should exist in a conventional Hall-bar (or multiple terminal) structure as there some debates (Brey and Fertig, 2014; Chu et al., 2011; Lee, 2009; Vafek, 2011; Zhang et al., 2012). In this case, the finite-size confinement-induced gap ($\sim \hbar v_F/t$, which is the energy separation between different sub-bands on side surfaces) is comparable to the 0–1 LL gap $v_F\sqrt{2eB\hbar}$ on the top and bottom surfaces. A schematic band structure belong this scenario is depicted in the upper panel of Fig. 25A, which shows the Fermi energy E_{f} residing inside the 0–1 LL gap and corresponds to $\nu_{\mathrm{t}} = 1/2$ and $\nu_{\mathrm{b}} = 1/2$ (the two surfaces are set to be degenerate with $V = 0$ here). The Fermi level passes though some non-chiral edge modes (in pairs) and chiral edge modes. It has been suggested that the QHE should be spoiled by those non-chiral edge modes in a standard Hall-bar measurement (Brüne et al., 2011; Vafek, 2011; Zhang et al., 2012). In our measurement setup (a conventional Hall-bar structure), the contacts connect to the top, bottom and side surfaces, all of which are probed simultaneously. However, for BSTS sample in a wide range of thickness ($\sim$10 to $\sim$100 nm, from similar to much larger than the magnetic length $l_{\mathrm{B}} \sim 6$ nm at $B = 18$ T), we do observe well-defined QHE. The behavior is similar to what expected for the scenario of $t \ll l_B$. This suggests that the non-chiral edge modes might be canceling each other and become

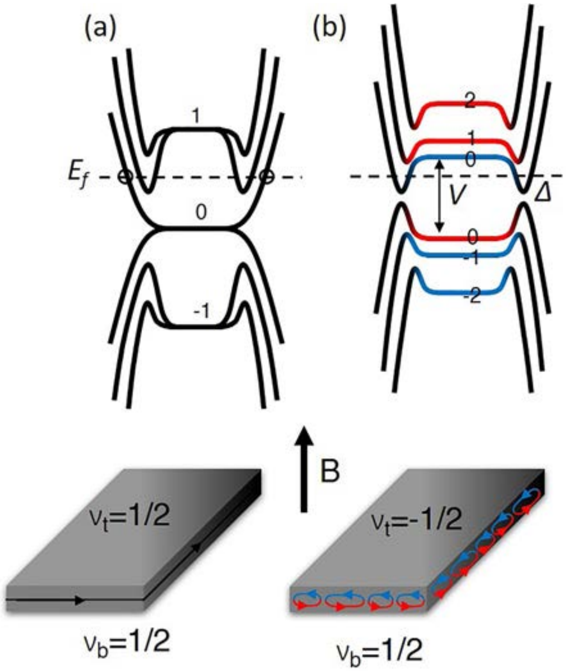

Fig. 25 (A) and (B) Schematics of surface band structures (upper), showing Landau levels from top and bottom surfaces (blue and red) in the middle of the sample transitioning into side surface sub-bands at sample edge, and edge states in a slab-shaped sample (lower) for $\nu = 1$ (A) and $\nu = 0$ (B) states. The dashed line indicates a representative Fermi level E_f and circles in (A) upper label chiral edge modes.

localized when net chiral modes exist, restoring the QHE (Brey and Fertig, 2014). However, in order to show well-defined QHE, the upper limit of t/l_B is not known yet. Certainly there has no QHE observed in bulk 3D TI samples ($t >$ a few μm).

When the two surfaces have opposite carrier types but one of them dominates, well-defined QH states with $\nu = \nu_t + \nu_b$ may still be observed, such as the (−1/2, 3/2) state with $\sigma_{xy} = (-1/2 + 3/2)\ e^2/h = e^2/h$ and vanishing ρ_{xx}. Previous studies in InAs/(AlSb)/GaSb heterostructure based electron-hole systems (Mendez et al., 1985; Suzuki et al., 2003) also revealed QH effect with $R_{xy} = h/(\nu e^2) = h/(\nu_e – \nu_h)e^2$ (ν_e and ν_e are electron and hole filling factors, both are positive integers) and vanishing R_{xx} when the AlSb barrier (separating electron and hole gases) is sufficiently thin to enable electron-hole hybridization. Despite the phenomenologically similarities, our QH system is distinctive in the sense that the spatially separated electrons and holes residing on the top and bottom surfaces have half-integer filling factors, and the hybridization only happens at the side surface.

For the $(\nu_t, \nu_b) = (-1/2, 1/2)$ or $(1/2, -1/2)$ state, the carrier density on the top and bottom surfaces are opposite. Since E_f is within the LL gap on both the surfaces, the finite residual σ_{xx} and large R_{nl} we observed are indicative of dissipative edge transport. We show a schematic energy spectrum (Morimoto et al., 2015a) of this $\nu = 0$ state with V slightly smaller than E_{0-1} in the upper panel of Fig. 25B, where the Fermi level E_f resides between the $N_t = -1$ and 0 LL of top surface (marked in blue), thus $\nu_t = -1/2$, and also between the $N_b = 0$ and 1 LL of bottom surface, thus $\nu_b = 1/2$. Overall, such energy spectrum represents a $(\nu_t, \nu_b) = (-1/2, 1/2)$ and $\nu = 0$ state. The E_f crosses an even number (only two shown in this illustrative example in Fig. 25B) of counter-propagating edge modes (arising from sub-bands of the quasi-1D side surface). The disorder can cause scattering and local equilibrium between the counter-propagating modes, giving rise to non-chiral dissipative transport (depicted by a series of conducting loops that can hop between adjacent ones in Fig. 25B lower panel) on the side surface with a large and finite resistance. While the energy spectrum (Fig. 25B) is expected to have a gap (Δ) near the edge (due to the hybridization between top (marked with blue) and bottom (red) surface zeroth LLs and approximately the finite-size confinement-induced gap $\approx hv_F/t \approx 10\,\mathrm{meV}$ opened at DP of the side surface (Morimoto et al., 2015a)), we did not observe a truly insulating state with vanishing σ_{xx} and diverging R_{xx} (Figs. 21A and 23A). This is likely due to the disorder potential (spatial fluctuation of DP (Beidenkopf et al., 2011)) comparable or larger than Δ and thus smearing out this gap (effectively E_f always crosses the non-chiral edge modes). It would be an interesting question for future studies to clarify whether the weak T-dependence (at $T < \sim 50\,\mathrm{K}$) of the observed conductance (Fig. 24A), similar to the behavior reported in InAs/GaSb based electron-hole systems (Takashina et al., 2003), may indicate an absence of localization (Anderson, 1958; Dunlap et al., 1989; Kurkijärvi, 1973; Lee, 1984) in such quasi-1D resistive edge channels.

Several recent theories have pointed out that the $\nu = 1/2 - 1/2 = 0$ state in the TI QH system may bring unique opportunities to realize various novel physics. It has been suggested that both the $\nu = 0$ state in TI QHE and an analogous quantum anomalous Hall (QAH) state with zero-Hall-conductance plateau in a magnetic doped TI around the coercive field can be used as platforms to observe the TME effect (Morimoto et al., 2015b; Wang et al., 2015), where an electric (magnetic) field induces a co-linear magnetic (electric) polarization with a quantized magnetoelectric polarizability of $\pm e^2/2h$. A zero-Hall-plateau state has been recently observed in the QAH case in ultrathin (few-nm-thick) films of $Cr_x(Bi,Sb)_{2\text{-}x}Te_3$ at low temperature (<1 K) (Feng et al., 2015; Kou et al., 2015). In comparison, our samples have much larger thickness (>~50 nm, suggested to be preferable for better developed TME effect (Baasanjav et al., 2014; Wang et al., 2015)), and our $\nu = 0$ state survives at much higher temperatures (~50 K). It has also been proposed that excitonic condensation and superfluidity can occur in thin 3D TIs at the $\nu = 0$ state in QH regime (Tilahun et al., 2011) (in addition to at zero B field (Seradjeh et al., 2009)) induced by spontaneous coherence between strongly-interacting top and bottom surfaces. In future studies, much thinner samples are likely needed to investigate the possibility of such exciton superfluidity.

4. Inter-surface hybridization in thin BSTS

In a relatively thick 3D TI film (thickness $t \gg 10$ nm), the top and bottom surfaces are well separated and their corresponding topological SS Dirac cones are gapless with opposite spin helicities. When the sample is thin enough (typically $\leq \sim 10$ nm) to enable hybridization between the two surfaces, a gap Δ_0 is opened at the Dirac point (even though the TRS is still preserved). The SS band structure acquires massive Dirac dispersion $\varepsilon = \pm\sqrt{(\hbar v_F \boldsymbol{k})^2 + (\Delta_0/2)^2}$ (Zhang et al., 2010). Schematics are shown in Fig. 26. Such a crossover of 3D TIs to the two-dimensional (2D) limit is little explored by electronic transport measurements in surface-dominant 3D TI systems (such as BSTS).

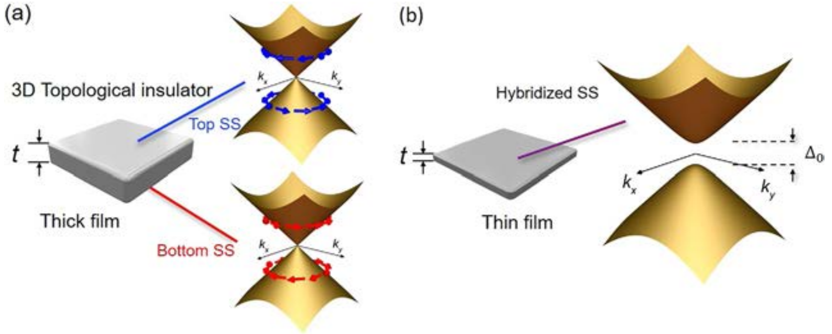

Fig. 26 (A and B) Schematics of the two surface Dirac cones with opposite spin helicities for a relatively thick TI sample (A) and the gapped surface band structure due to the hybridization of top and bottom SS for a very thin TI sample (B). The gap size at zero field is denoted as Δ_0.

In this section, we discuss about the inter-surface hybridization effect in dual-gated BSTS thin samples, upon which we can electrostatically control both surfaces to the charge neutrality point. By reducing the thickness of the BSTS flake, the capacitive coupling between the two surfaces becomes stronger (Fatemi et al., 2014; Kim et al., 2012a). As it can be seen in the color map of 2D conductivity ($\sigma_{xx}=L/(W^*R_{xx})$) vs V_{tg} and V_{bg}, the black and white dashed lines tracing the Dirac points of top and bottom surfaces cross and tend to merge together when the thickness t is reduced from 80 to 17 nm (Fig. 27A and B). Further reducing t to ~10 nm results in the Dirac points from the two surfaces to become indistinguishable (Fig. 27C). When the sample is only a few nm thick (e.g., Device N4 with $t=6$ nm in Fig. 27D), a hard gap opens, as indicated by the highly insulating (two-terminal conductivity $\sigma \ll e^2/h$) blue region at $T=1.6$ K.

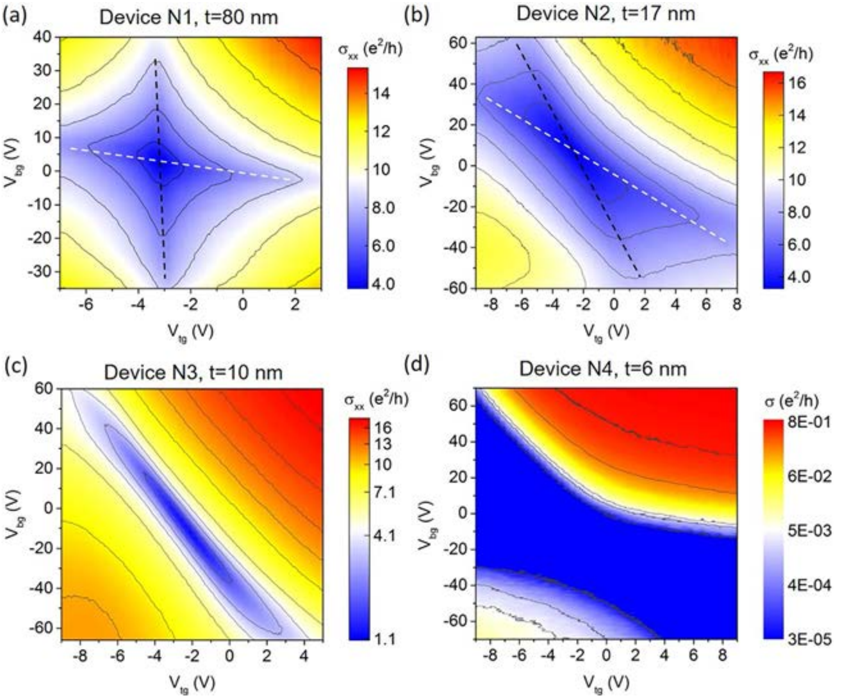

Fig. 27 (A–D) Measured conductivities (in color scale, with contours) as functions of top and backgate voltages (V_{tg} and V_{bg}) in four representative devices with decreasing thickness (t). In relatively thick samples N1 (A) and N2 (B), the dashed black and white lines are guides to the eyes indicating the top and bottom surface charge neutrality Dirac points, respectively. Data are measured at temperature $T=0.35$ K in (A–C), and at $T=1.6$ K in (D). All data in this paper are measured with a 4-terminal configuration except for devices thinner than 7 nm (such as N4), which are measured with a 2-terminal configuration.

The minimum conductivity σ_{min} and maximum resistivity ρ_{max} ($=1/\sigma_{\mathrm{min}}$) are reached when the two surfaces are gated simultaneously to charge neutrality points or Dirac points. In Fig. 27A, we plotted ρ_{max} as a function of temperature (T) for a few representative samples. At $t > 10\,\mathrm{nm}$, ρ_{max} shows a metallic behavior ($\mathrm{d}\rho_{\mathrm{max}}/\mathrm{d}T > 0$), implying a zero or negligible gap. However, at $t < 10\,\mathrm{nm}$, a strongly insulating behavior ($\mathrm{d}\rho_{\mathrm{max}}/\mathrm{d}T < 0$) is observed. Around $t = 10\,\mathrm{nm}$, different samples can behave differently. For example, while device N5 exhibits an insulating behavior, another device N3 exhibits a non-monotonic temperature dependence with its ρ_{max}(T) close to h/e^2 and separating curves with metallic and insulating behaviors. It is consistent with the general observation from previous studies that the critical resistivity for a metal–insulator transition in 2D electron systems is on the order of the resistance quantum h/e^2.

In Fig. 28B, we replotted four representative data sets from Fig. 28A as σ_{min} vs $1/T$. The size of non-zero effective transport gap Δ_0* in thinner BSTS samples is estimated from thermal activation fit with $\rho_{max} \propto e^{\Delta_0^*/2k_BT}$ or $\sigma_{min} \propto e^{-\Delta_0^*/2k_BT}$ in appropriate temperature ranges, beyond which other conduction mechanisms need to be considered to describe the temperature-dependent conduction. For example, in samples with $t = 10\,\mathrm{nm}$ (Device N3 and N5) and 8 nm, the thermal activation fit has been applied to the temperature range between ~3 to ~30 K, where an insulating behavior is observed, to extract Δ_0* (note that it could be smaller than the real hybridization gap Δ_0 due to smearing effect of potential fluctuations at different positions). This temperature range is chosen for the following reasons. Usually below 3 K, σ_{min} tends to deviate from a single thermal activation fit. As shown in Fig. 28C of a typical example N5, we can fit the temperature dependent data down to 0.3 K with an empirical formula $\sigma_{min} = C_1 e^{-T_1/T} + C_2 e^{-(T_2/T)1/3}$, which gives $T_1 = \sim 8\,\mathrm{K}$ and $T_2 = \sim 0.02\,\mathrm{K}$. The second term has the form of variable range hopping (VRH) for 2D (we caution that other forms may be used that also give reasonable fits), suggesting multiple conduction mechanisms at lower temperatures. Above ~30 K, Dirac points usually shift and the peak become much broader in gate voltage sweeps, indicating additional conducting channels such as impurities or bulk states.

In Fig. 28D, we showed the thermal activation fit for another 6 nm-thick device in the temperature range of 76 to ~300 K, below which σ_{min} becomes too small to be detected accurately due to limitation of our instruments. The good linearity of σ_{min} in logarithmic scale vs $1/T$ indicates a hard gap opening in this device and the fitting gives a gap size ~160 meV, which is much larger than that determined by ARPES measurements

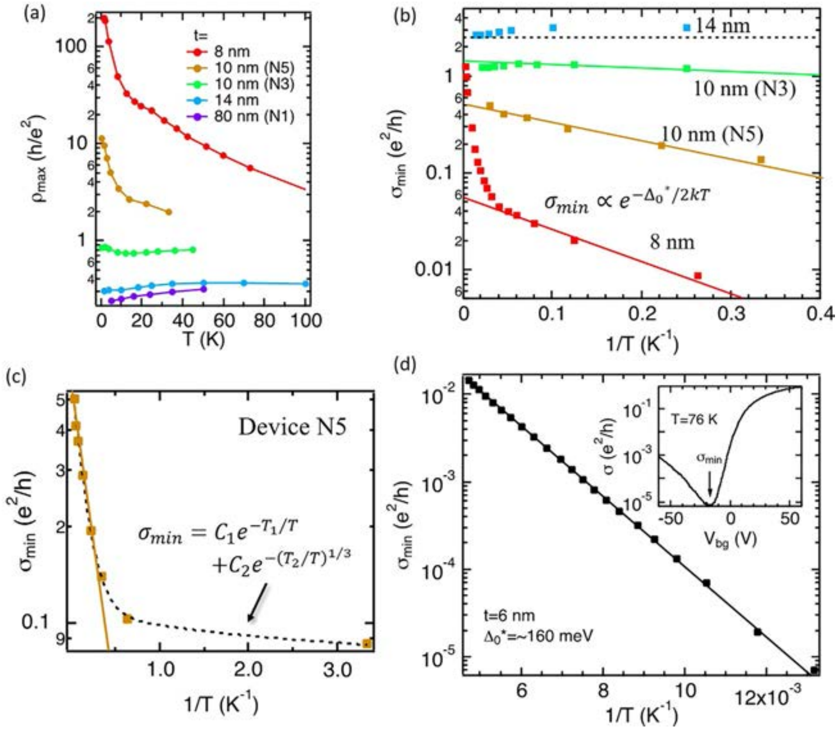

Fig. 28 (A) Temperature dependence of ρ_{max} in log scale for five representative devices. (B) Same data from (A) replotted as minimum conductivity σ_{min} vs 1/T for four BSTS samples. The solid lines are the thermal activation fits for the corresponding thin samples (typically in the temperature range between 3 and 30K). The dashed horizontal line is a guide to the eye for a thicker (14nm) sample showing an opposite trend compared to the thin ones, indicating a metallic behavior and a zero gap. (C) The σ_{min} vs $1/T$ for Device N5 (10nm thick) in a larger temperature range (down to 0.3K). The yellow solid line is the same thermal activation fit in (B) for higher temperatures while the dashed curve is a fit based on the formula shown in the (C) for the whole temperature range. (D) In a 6-nm-thick sample, thermal activation fits well in the entire temperature range (76 to 300K), giving a gap size of 160meV. Inset is a typical backgate dependence for the 2-terminal conductivity measured at 76K for this device.

on 6nm Bi_2Se_3 grown by molecular beam epitaxy (MBE, surface gap barely vanishes at 6nm) (Zhang et al., 2010) and the theory prediction for Bi_2Se_3 (a few meV at 6nm) (Linder et al., 2009; Liu et al., 2010). A much enhanced gap size has also reported previously on exfoliated Bi_2Se_3 thin flakes (Cho et al., 2011). Given the material difference and better isolated surface conduction, the gap size in our thin BSTS films grows monotonically with reducing thickness and roughly follow an exponential function $\Delta_0{*}\propto e^{-0.7t/[\mathrm{nm}]}$) (Fig. 29 inset). The Δ_0* grows by about an order

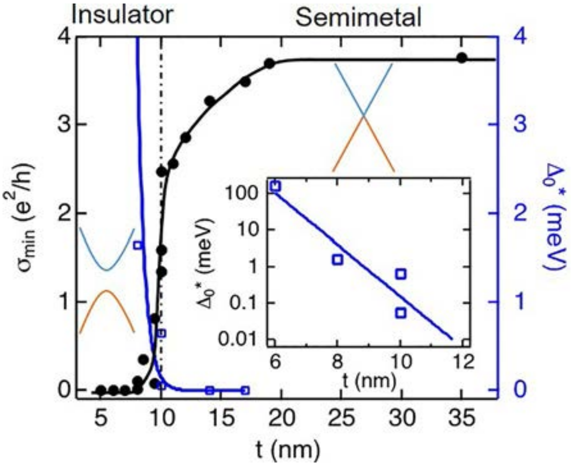

Fig. 29 The σ_{min} ($=1/\rho_{max}$, left axis) at low T (<2 K) and the gap size Δ_0^* (right axis) as functions of sample thickness t. The dashed-dotted vertical line marks the critical thickness $t_c = \sim 10$ nm that separates the semimetal ($t > t_c$, corresponding to the 3D TI phase in the inset with gapless Dirac SS) and insulator ($t \leq t_c$, corresponding to the trivial insulator phase in the inset with hybridized and gapped SS) behaviors. The inset plot shows Δ_0^* in log scale vs t and an exponential fitting.

of magnitude when t is reduced by $\sim$1.4 nm, comparable to what was found for Bi_2Se_3 (Kim et al., 2013; Zhang et al., 2010). We don't have evidence of oscillatory behavior of Δ_0^* vs t and did not observe any signs of quantum spin Hall effect (Linder et al., 2009; Liu et al., 2010; Lu et al., 2010).

Fig. 29 shows σ_{min} at base temperatures ($T \leq 1.6$ K) for samples with various thicknesses. At large t ($> \sim 20$ nm), saturates around a value close to $4e^2/h$ (Xu et al., 2016). The σ_{min} starts to decrease below 20 nm and drops abruptly to zero below $\sim$10 nm. The gap size Δ_0^* extracted from thermal activation is plotted on the right axis of Fig. 28.

Our data suggest that a measurable transport gap Δ_0^* (presumably driven by the inter-surface hybridization) opens at the Dirac point below a critical thickness $t_c = 10 \pm 1$ nm in our samples.

5. In-plane magnetic field effect

5.1 Effect of an in-plane magnetic field on relatively thick samples

Resistances of the thicker and thinner samples respond to the in-plane magnetic field differently at low temperatures. For consistency, the samples are mounted with current direction parallel to B (unless otherwise specified).

We have measured multiple samples by either sweeping V_{tg} (with V_{bg} carefully tuned and then fixed at voltages such that these V_{tg} sweeps go through maximum resistivity ρ_{max}) at different in-plane B fields, or measuring ρ_{max} vs in-plane B at fixed gate voltages. For relatively thick samples such as Device N2 (dual-gating effect at zero field seen in last Chapter) with $t = 17\,\text{nm} > t_c$, the in-plane field up to ~31 T only induced a relatively small positive MR of ~40% (Fig. 30, noting $\rho_{max}(B)$ is approximately proportional to B^2 at low fields and proportional to B at higher fields). We also noticed that with increasing B field, there is a crossover from the metallic to non-metallic behavior (seen from the temperature dependence of the data at fixed fields, with two examples at 0 and 31.5 T shown in the inset of Fig. 30D) at 6 T.

In relatively thick samples, we shouldn't expect any MR effect with the in-plane magnetic field as its contribution to the Hamiltonian can be

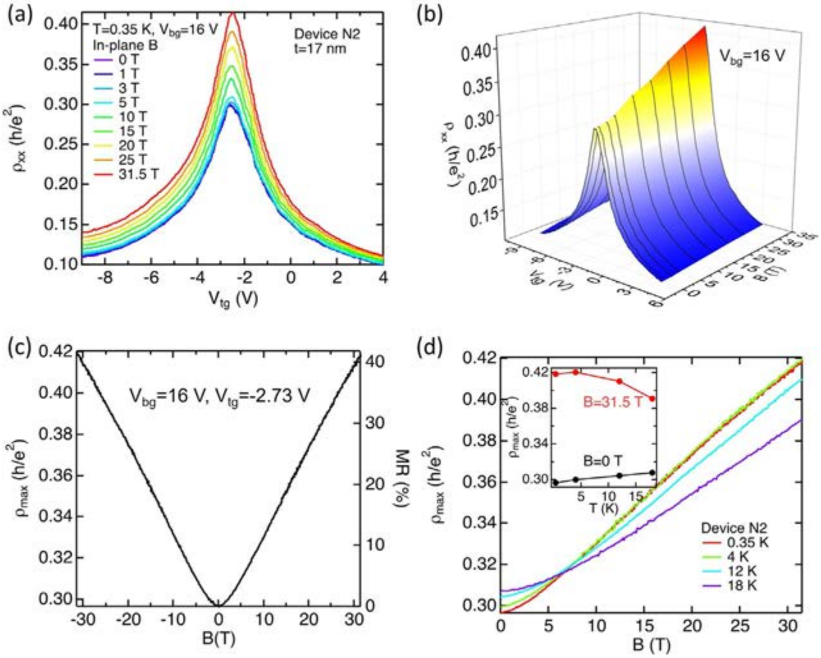

Fig. 30 (A and B) Resistivity of Device N2 measured as a function of the top-gate voltage (V_{tg}) at various in-plane B fields at $T = 0.3$ K, where (A) is the raw data set while (B) is the generated 3D contour plot. The corresponding V_{bg}'s are carefully tuned such that the V_{tg} sweeps go through the global resistivity maximum ρ_{max}. (C and D) The ρ_{max} (and the corresponding MR, right axis) measured (at fixed V_{bg} and V_{tg} labeled in the figure) as a function of in-plane B field measured at $T = 0.3$ K (C) and multiple temperatures (D).

eliminated by a gauge transformation. The small positive MR observed here are of interests for future studies and could be related to magnetic field induced spin-flip scattering process (Taskin et al., 2017).

5.2 Large negative MR in thinner samples

In this section, we'll mainly focus on the in-plane measurements on thinner devices N3 and N5 (see an optical image in Fig. 31A and B) both with thickness around 10 nm. At zero field, Device N5 shows maximum resistivity $\rho_{\max}$ near $V_{bg} \approx 30\,V$ and $V_{tg} \approx 1\,V$ (note that depending on gate sweep histories, the exact peak position could vary slightly) at zero field and base temperature $T = 0.3\,K$.

At small in-plane fields (<~5 T), devices N3 and N5 also show some positive MR (for N5, we also observed an additional tiny cusp with negative MR near 0 T, see Fig. 32). Such low-field features in thinner devices disappear when we increase the temperature to just a few Kelvin (see Fig. 33), thus are attributed to phase coherent transport (Liao et al., 2015; Lin et al., 2013). In the following, we mainly focus on the higher magnetic field data showing a giant negative MR that has only been observed in thin samples with insulating behavior. For example, in Device N3 (Fig. 32A and B), $\rho_{\max}$ drops dramatically above ~5 T and saturates at high field (~30 T)

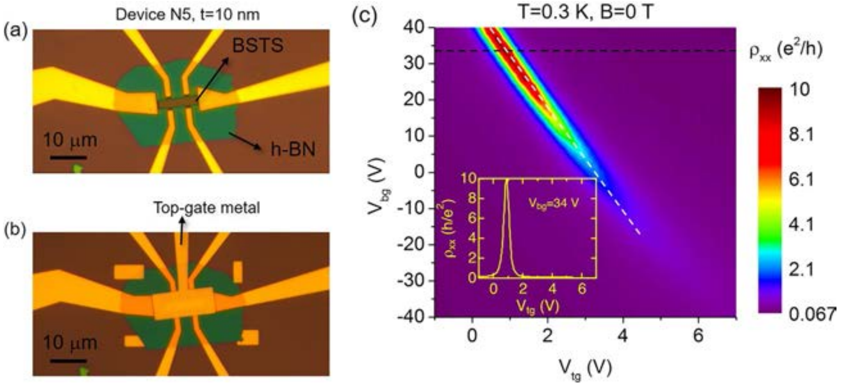

Fig. 31 (A and B) Optical images for the BSTS device N5 before and after top-gate metal deposition. The BSTS flake is etched into a Hall-bar structure and covered with a hexagonal boron nitride (h-BN) flake (~24 nm thick) as top-gate dielectric. (C) The ρ_{xx} as a function of V_{bg} and V_{tg} for Device N5. The behavior is similar to that of Device N3 with resistivity peak along the total charge neutral line (dashed white line). However, Device N5 is initially more n doped and has a larger $\rho_{\max}$ (~10 h/e^2) as identified from the maximum resistivity peak in the line cut (shown in the inset) along the dashed line near $V_{bg} = 34\,V$.

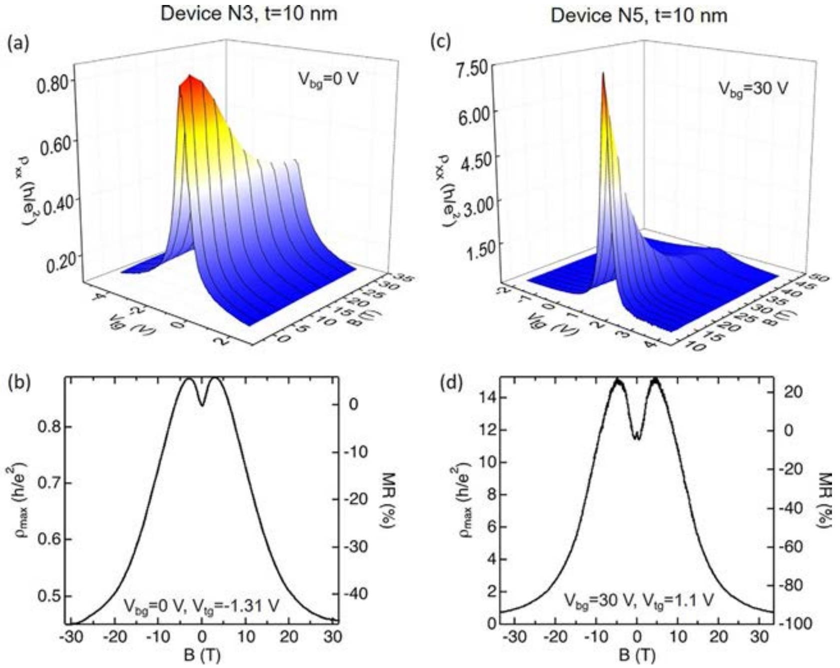

Fig. 32 (A and C) Resistivity of three representative devices (N3 and N5) measured as a function of the top-gate voltage (V_{tg}) at various in-plane B fields at $T=0.3\,\mathrm{K}$. The corresponding V_{bg}'s are carefully tuned such that the V_{tg} sweeps go through the global resistivity maximum max. (B,D) The ρ_{max} (and the corresponding MR, right axis) measured (at fixed V_{bg} and V_{tg} labeled in the figure) as a function of in-plane B field for the two devices (N3 and N5, respectively).

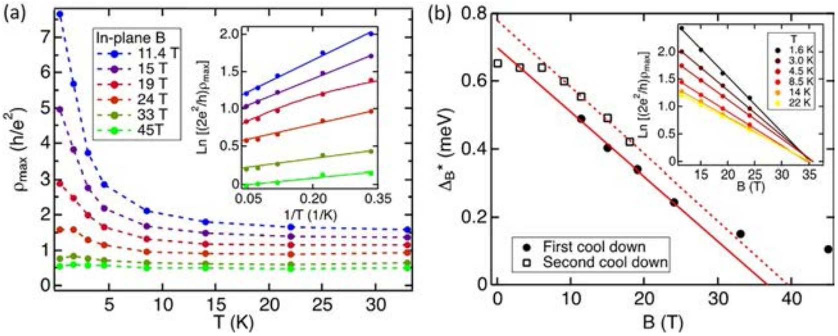

Fig. 33 (A) The ρ_{max} of device N5 ($t\sim 10\,\mathrm{nm}$) as a function of temperature at different in-plane B from 11.4 up to 45 T. Inset shows the corresponding thermal activation fittings, while the extracted $\Delta_B{}^*$ is plotted (filled circles) as a function of B in (B) along with data measured from another (second) cool down. (B) The linear fits for both cool downs (solid and dash lines, respectively) indicate a gap closing at B_c between 35 and 40 T, consistent with the inset showing the converging (at $B_c=36\,\mathrm{T}$) of all the linear fittings from Ln[$(2e^2/h)\rho_{max}$] vs B at different temperatures.

to $\sim 0.45\,h/e^2$. Notably for the more insulating sample N5 (Fig. 32C and D), $\rho_{\max}$ drops by a factor of ~ 20 (giving an MR $\sim 95\%$) from a very resistive value of $\sim 12h/e^2$ at $B = 0\,\mathrm{T}$ to a value ($\sim 0.55h/e^2$) again close to $h/2e^2$ at $B = 45\,\mathrm{T}$.

5.3 In-plane magnetic field induced insulator-semimetal transition

We performed systematic V_{tg} sweeps (fixed $V_{\mathrm{bg}} = 30\,\mathrm{V}$) to extract $\rho_{\max}$ with in-plane B fields from 11.4 to 45 T in Device N5 at various temperatures. As shown in Fig. 33A, the insulating behavior of $\rho_{\max}(T)$ is strongly suppressed at higher fields. At the highest field (45 T), $\rho_{\max}$ saturates to a value close to $\sim \mathrm{h}/2\mathrm{e}^2$ and becomes relatively insensitive to temperature. We estimated the thermal activation gap $\Delta_B{}^*$ at each B field from the slope of $\mathrm{Ln}[(2\mathrm{e}^2/\mathrm{h})\rho_{\max}]$ vs $1/T$ in the temperature range of 3 to 22 K (Fig. 33A inset) and plotted it vs the corresponding B in Fig. 33B, which also displays the gap size measured in another (second) cool down for B up to 18 T. The gap size $\Delta_B{}^*$ is found to differ slightly over different cool downs but exhibits a similar linear dependence on B in the intermediate field range ($5\,\mathrm{T} \sim 30\,\mathrm{T}$).

Extrapolating the linear fits in Fig. 33B to zero suggests that the gap would close at a critical field (B_c) between 36 to 40 T, around which we observe the sample (N5) to become metallic ($d\rho_{\max}/dT > 0$, see Fig. 33A) below $T \sim 2\,\mathrm{K}$. However, some non-metallic behavior ($d\rho_{\max}/dT < 0$) can still be observed between 2 to 22 K even at the highest fields (Fig. 33A) and fitted to a thermal activation, giving $\Delta_B{}^*$ that deviates from the red solid line (Fig. 33B). A non-metallic behavior under large in-plane magnetic fields was also observed in gapless samples such as N2 with $t = 17\,\mathrm{nm}$ (Fig. 30D) The reason for this behavior remains to be understood (note a hybridization gap opening is not expected in such thick samples). We have also verified that $\mathrm{Ln}[(2\mathrm{e}^2/\mathrm{h})\rho_{\max}]$ is linear with B ($<\sim 25\,\mathrm{T}$) at different temperatures and all the fitted lines converge to a critical field of $B_c \sim 36\,\mathrm{T}$ (inset of Fig. 33B). This also suggests $\Delta_B{}^* \propto (B_c - B)$, with a saturation resistivity $\sim \mathrm{h}/2\mathrm{e}^2$ (when $\Delta_B{}^* \sim 0$) and gap closing at $B_c \sim 36\,\mathrm{T}$ at fixed temperatures.

5.4 Discussion

Such large negative MR and the corresponding insulator-semimetal transition have not been reported before in thin nonmagnetic 3D TIs with surface dominant conduction. The relatively small negative MR previously shown in Bi_2Se_3 with in-plane magnetic fields are attributed to bulk carriers and can be understood by semiclassical Boltzmann formalism considering the Berry curvature and orbital moment of the bulk states (Dai et al., 2017). Our observations of distinct behavior between thick and thin BSTS samples may be interpreted in terms of a theoretical prediction by Zyuzin et al. (2011). Generally, in thick TIs the in-plane magnetic field B (set to be along the x direction) can introduce opposite shifts (along k_y) of top and bottom surface Dirac cones in the momentum space. This does not produce any MR effect in thick 3D TIs but will prevent the two Dirac points from annihilation and eliminate the hybridization gap in thin TIs (schematics shown in Fig. 34A). Semiclassically, a spin-helical SS electron with spin orientated along the B field (thus spin magnetic moment $-g\mu_B/2$, with g being the in-plane spin g-factor and $\mu_B \approx 0.058\,\text{meV/T}$ the Bohr magneton) moves

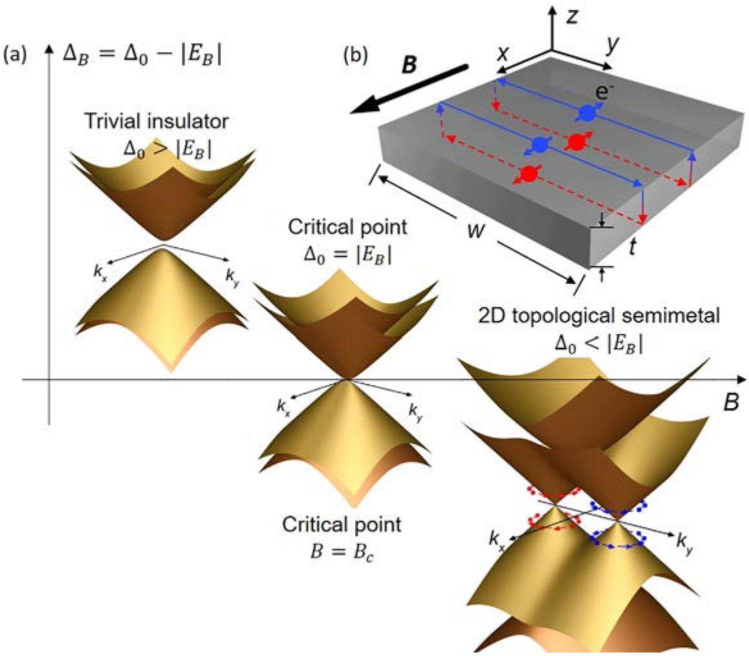

Fig. 34 (A) Predicted evolution of the surface band structure from a trivial insulator toward a 2D topological semimetal (TSM), upon increasing in-plane B field in a thin TI sample with hybridized SS. The gap Δ_B decreases linearly with B and is closed when $\Delta_0 = |E_B|$, where $E_B = (g\mu_B\text{-}etv_F)B$. Red/blue arrows depict spin textures of the gapless Dirac cones, separated in the momentum space for 2D TSM, respectively. (B) Schematic of the orbital motion (normal to $\boldsymbol{B}$ and x direction) of spin-helical SS electrons for a 3D TI film.

clockwise around the circumference (Fig. 34B) with orbital magnetic moment (parallel to B field) $\mu_{orb} = \frac{e}{2(w+\ t)/v_F} \bullet wt \approx etv_F/2$ (noting width $w >> t$ in our samples) (Minot et al., 2004). Both the spin and orbital magnetic moments couple to the B field, giving rise to an effective Zeeman energy $E_B = g_{eff}\mu_B B = (g\mu_B - etv_F)B$ (total effective $g_{eff} = g - etv_F/\mu_B$, the second term can also be considered as due to the Aharonov-Bohm phase gradient between the two opposite surfaces). In thin TIs with hybridization gap Δ_0 (at zero B field), one can show (Zyuzin et al., 2011) that the massive Dirac band is spin-split by the above "effective Zeeman energy," shrinking the hybridization gap linearly with B as $\Delta_B = \Delta_0 - |E_B|$. The gap vanishes at a critical field B_c ($|E_B| = \Delta_0$), where the dispersion near $\boldsymbol{k} = 0$ becomes quadratic along k_y and linear along k_x (see Fig. 34A). With further increasing B ($> B_c$), two Dirac points are restored and separated by $\sqrt{E_B^2 - \Delta_0^2}/\hbar v_F$ along k_y. This gives rise to a distinct 2D TSM that is topologically stable as long as translational symmetry is preserved (Zyuzin et al., 2011).

The above mechanism can qualitatively explain the trend we observed in experiments. However, the slope of the linear fitting yields the gap closing rate $|\frac{E_B}{B}| \approx$ 0.02 meV/T (corresponding to $|g_{eff}| \approx 0.33$). This is nearly two orders of magnitudes smaller compared with $|\frac{E_B}{B}| \sim 1$ meV/T estimated for a 10-nm sample by Zyuzin et al., 2011, which assumed $g = 2$, leading to a negligibly small contribution from the Zeeman effect. Our results imply a large g, giving rise to a Zeeman term ($g\mu_B B$) that is comparable with the orbital term ($etv_F B$). Thus, the two nearly cancel to give a small $|\frac{E_B}{B}|$, which can be used to extract the in-plane SS g-factor if the Fermi velocity v_F is known. Assuming a typical $v_F = 3.5 \times 10^5$ m/s for topological SS with purely linear dispersion, we get a g-factor of ~60. In actual 3D TI materials such as BSTS, the surface Dirac cone contains substantial nonlinearity that can be described by a quadratic mass term added to the SS Hamiltonian. Subsequently, a reduced $v_F = 1.3 \times 10^5$ m/s, which describes the linear part in the Hamiltonian, yields a g-factor of ~20. It has been pointed out that the Zeeman coupling of the SS carriers can be highly anisotropic (Chu et al., 2011). In previous experiments, only an out-of-plane SS g-factor is determined and found to vary significantly in different TI materials (Fu et al., 2016; Taskin and Ando, 2011). Our study provides a method to extract the *in-plane* g-factor of SS carriers. We have to note that in our experiments, the gap extracted from thermal activation is an effective transport gap ($\Delta_B{}^*$) and can be smaller than the real band gap (Δ_B) due to disorder-induced smearing, namely $\Delta_B^* = \Delta_B - \delta$, where δ is a correction due to the potential fluctuations (likely to be on the order of several meV or higher (Nam et al., 2019)) in the system. Therefore, the observed apparent metallic behavior (Δ_B^* reaching 0) in Device N5 above $B_c \sim 36\,\mathrm{T}$ does not necessarily indicate the realization of the 2D TSM phase, which requires closing the real gap Δ_B and possibly much larger magnetic field than B_c (noting the relatively small gap closing rate of 0.02 meV/T in light of the estimated $\delta \sim$ meV in our BSTS samples). It might be easier to realize the 2D TSM phase (at lower B field) in other TI systems with a smaller or even negative g-factor (so the gap closing rate can be much larger than that in our samples). It would also be interesting for future studies to clarify whether the saturation resistivity $\sim h/2e^2$ is related to the modification of band structure and magnetic field induced spin-flip scatterings (Lin et al., 2013).

References

Analytis, J.G., McDonald, R.D., Riggs, S.C., Chu, J.-H., Boebinger, G.S., Fisher, I.R., 2010. Two-dimensional surface state in the quantum limit of a topological insulator. Nat. Phys. 6, 960–964. https://doi.org/10.1038/nphys1861.

Anderson, P.W., 1958. Absence of diffusion in certain random lattices. Phys. Rev. 109, 1492–1505. https://doi.org/10.1103/PhysRev.109.1492.

Arakane, T., Sato, T., Souma, S., Kosaka, K., Nakayama, K., Komatsu, M., Takahashi, T., Ren, Z., Segawa, K., Ando, Y., 2012. Tunable Dirac cone in the topological insulator Bi2-xSb xTe3-ySey. Nat. Commun. 3, 636. https://doi.org/10.1038/ncomms1639.

Armitage, N.P., Mele, E.J., Vishwanath, A., 2018. Weyl and Dirac semimetals in three-dimensional solids. Rev. Mod. Phys. 90, 015001. https://doi.org/10.1103/RevModPhys.90.015001.

Baasanjav, D., Tretiakov, O.A., Nomura, K., 2014. Magnetoelectric effect in topological insulator films beyond the linear response regime. Phys. Rev. B 90, 045149. https://doi.org/10.1103/PhysRevB.90.045149.

Beidenkopf, H., Roushan, P., Seo, J., Gorman, L., Drozdov, I., Hor, Y.S., Cava, R.J., Yazdani, A., 2011. Spatial fluctuations of helical Dirac fermions on the surface of topological insulators. Nat. Phys. 7, 939–943. https://doi.org/10.1038/nphys2108.

Bernevig, B.A., Zhang, S.C., 2006. Quantum spin hall effect. Phys. Rev. Lett. 96, 106802. https://doi.org/10.1103/PhysRevLett.96.106802.

Brey, L., Fertig, H.A., 2014. Electronic states of wires and slabs of topological insulators: quantum Hall effects and edge transport. Phys. Rev. B 89, 085305. https://doi.org/10.1103/PhysRevB.89.085305.

Brüne, C., Liu, C.X., Novik, E.G., Hankiewicz, E.M., Buhmann, H., Chen, Y.L., Qi, X.L., Shen, Z.X., Zhang, S.C., Molenkamp, L.W., 2011. Quantum hall effect from the topological surface states of strained bulk HgTe. Phys. Rev. Lett. 106, 126803. https://doi.org/10.1103/PhysRevLett.106.126803.

Burkov, A.A., Balents, L., 2011. Weyl semimetal in a topological insulator multilayer. Phys. Rev. Lett. 107, 127205. https://doi.org/10.1103/PhysRevLett.107.127205.

Büttner, B., Liu, C.X., Tkachov, G., Novik, E.G., Brüne, C., Buhmann, H., Hankiewicz, E.M., Recher, P., Trauzettel, B., Zhang, S.C., Molenkamp, L.W., 2011. Single valley Dirac fermions in zero-gap HgTe quantum wells. Nat. Phys. 7, 418–422. https://doi.org/10.1038/nphys1914.

Cao, H., Tian, J., Miotkowski, I., Shen, T., Hu, J., Qiao, S., Chen, Y.P., 2012. Quantized hall effect and shubnikov-de haas oscillations in highly doped Bi2Se3: evidence for layered transport of bulk carriers. Phys. Rev. Lett. 108, 216803. https://doi.org/10.1103/PhysRevLett.108.216803.

Chadov, S., Qi, X., Kübler, J., Fecher, G.H., Felser, C., Zhang, S.C., 2010. Tunable multifunctional topological insulators in ternary Heusler compounds. Nat. Mater. 9, 541–545.

Chang, C.-Z., Zhang, J., Feng, X., Shen, J., Zhang, Z., Guo, M., Li, K., Ou, Y., Wei, P., Wang, L.-L., Ji, Z.-Q., Feng, Y., Ji, S., Chen, X., Jia, J., Dai, X., Fang, Z., Zhang, S.-C., He, K., Wang, Y., Lu, L., Ma, X.-C., Xue, Q.-K., 2013. Experimental observation of the quantum anomalous Hall effect in a magnetic topological insulator. Science 340, 167–170. https://doi.org/10.1126/science.1234414.

Chen, J.-H., Jang, C., Adam, S., Fuhrer, M.S., Williams, E.D., Ishigami, M., 2008. Charged-impurity scattering in graphene. Nat. Phys. 4, 377–381. https://doi.org/10.1038/nphys935.

Chen, J., Qin, H., Yang, F., Liu, J., Guan, T., Qu, F., Zhang, G., Shi, J., Xie, X., Yang, C., Wu, K., Li, Y., Lu, L., 2010. Gate-voltage control of chemical potential and weak antilocalization in Bi2Se3. Phys. Rev. Lett. 105, 176602. https://doi.org/10.1103/PhysRevLett.105.176602.

Cho, S., Butch, N.P., Paglione, J., Fuhrer, M.S., 2011. Insulating behavior in ultrathin bismuth selenide field effect transistors. Nano Lett. 11, 1925–1927. https://doi.org/10.1021/nl200017f.

Chu, R.-L., Shi, J., Shen, S.-Q., 2011. Surface edge state and half-quantized Hall conductance in topological insulators. Phys. Rev. B 84, 085312. https://doi.org/10.1103/PhysRevB.84.085312.

Dai, X., Du, Z.Z., Lu, H.Z., 2017. Negative magnetoresistance without chiral anomaly in topological insulators. Phys. Rev. Lett. 119, 166601. https://doi.org/10.1103/PhysRevLett.119.166601.

Das Sarma, S., Adam, S., Hwang, E.H., Rossi, E., 2011. Electronic transport in two-dimensional graphene. Rev. Mod. Phys. 83, 407–470. https://doi.org/10.1103/RevModPhys.83.407.

Dean, C.R., Young, A.F., Meric, I., Lee, C., Wang, L., Sorgenfrei, S., Watanabe, K., Taniguchi, T., Kim, P., Shepard, K.L., Hone, J., 2010. Boron nitride substrates for high-quality graphene electronics. Nat. Nanotechnol. 5, 722–726. https://doi.org/10.1038/nnano.2010.172.

Dunlap, D.H., Kundu, K., Phillips, P., 1989. Absence of localization in certain statically disordered lattices in any spatial dimension. Phys. Rev. B 40, 10999–11006. https://doi.org/10.1103/PhysRevB.40.10999.

Dziawa, P., Kowalski, B.J., Dybko, K., Buczko, R., Szczerbakow, A., Szot, M., Łusakowska, E., Balasubramanian, T., Wojek, B.M., Berntsen, M.H., Tjernberg, O., Story, T., 2012. Topological crystalline insulator states in Pb1−xSnxSe. Nat. Mater. 11, 1023–1027. https://doi.org/10.1038/nmat3449.

Fatemi, V., Hunt, B., Steinberg, H., Eltinge, S.L., Mahmood, F., Butch, N.P., Watanabe, K., Taniguchi, T., Gedik, N., Ashoori, R.C., Jarillo-Herrero, P., 2014. Electrostatic coupling between two surfaces of a topological insulator nanodevice. Phys. Rev. Lett. 113, 206801. https://doi.org/10.1103/PhysRevLett.113.206801.

Feng, Y., Feng, X., Ou, Y., Wang, J., Liu, C., Zhang, L., Zhao, D., Jiang, G., Zhang, S.-C., He, K., Ma, X., Xue, Q.-K., Wang, Y., 2015. Observation of the zero hall plateau in a quantum anomalous hall insulator. Phys. Rev. Lett. 115, 126801. https://doi.org/10.1103/PhysRevLett.115.126801.

Fu, L., 2011. Topological crystalline insulators. Phys. Rev. Lett. 106, 106802. https://doi.org/10.1103/PhysRevLett.106.106802.

Fu, L., Kane, C.L., 2008. Superconducting proximity effect and majorana fermions at the surface of a topological insulator. Phys. Rev. Lett. 100, 096407. https://doi.org/10.1103/PhysRevLett.100.096407.

Fu, Y.-S., Hanaguri, T., Igarashi, K., Kawamura, M., Bahramy, M.S., Sasagawa, T., 2016. Observation of Zeeman effect in topological surface state with distinct material dependence. Nat. Commun. 7, 10829. https://doi.org/10.1038/ncomms10829.

Gao, B.F., Gehring, P., Burghard, M., Kern, K., 2012. Gate-controlled linear magnetoresistance in thin Bi2Se3 sheets. Appl. Phys. Lett. 100, 212402. https://doi.org/10.1063/1.4719196.

Giraud, S., Kundu, A., Egger, R., 2012. Electron-phonon scattering in topological insulator thin films. Phys. Rev. B 85, 35441. https://doi.org/10.1103/PhysRevB.85.035441.

Gusev, G.M., Olshanetsky, E.B., Kvon, Z.D., Levin, A.D., Mikhailov, N.N., Dvoretsky, S.A., 2012. Nonlocal transport near charge neutrality point in a two-dimensional electron-hole system. Phys. Rev. Lett. 108, 226804. https://doi.org/10.1103/PhysRevLett.108.226804.

Hasan, M.Z., Kane, C.L., 2010. Colloquium: topological insulators. Rev. Mod. Phys. 82, 3045–3067. https://doi.org/10.1103/RevModPhys.82.3045.

Heremans, J.P., Cava, R.J., Samarth, N., 2017. Tetradymites as thermoelectrics and topological insulators. Nat. Rev. Mater. 2, 17049. https://doi.org/10.1038/natrevmats.2017.49.

Hikami, S., Larkin, A.I., Nagaoka, Y., 1980. Spin-orbit interaction and magnetoresistance in the two dimensional random system. Prog. Theor. Phys. 63, 707–710. https://doi.org/10.1143/PTP.63.707.

Hor, Y.S., Richardella, A., Roushan, P., Xia, Y., Checkelsky, J.G., Yazdani, A., Hasan, M.Z., Ong, N.P., Cava, R.J., 2009. p-type Bi2Se3 for topological insulator and low-temperature thermoelectric applications. Phys. Rev. B 79, 195208. https://doi.org/10.1103/PhysRevB.79.195208.

Jabakhanji, B., Michon, A., Consejo, C., Desrat, W., Portail, M., Tiberj, A., Paillet, M., Zahab, A., Cheynis, F., Lafont, F., Schopfer, F., Poirier, W., Bertran, F., Le Fèvre, P., Taleb-Ibrahimi, A., Kazazis, D., Escoffier, W., Camargo, B.C., Kopelevich, Y., Camassel, J., Jouault, B., 2014. Tuning the transport properties of graphene films grown by CVD on SiC(0001): effect of in situ hydrogenation and annealing. Phys. Rev. B 89, 085422. https://doi.org/10.1103/PhysRevB.89.085422.

Kane, C.L., Mele, E.J., 2005. Z2 topological order and the quantum spin hall effect. Phys. Rev. Lett. 95, 146802. https://doi.org/10.1103/PhysRevLett.95.146802.

Kim, D., Cho, S., Butch, N.P., Syers, P., Kirshenbaum, K., Adam, S., Paglione, J., Fuhrer, M.S., 2012a. Surface conduction of topological Dirac electrons in bulk insulating Bi2Se3. Nat. Phys. 8, 460–464. https://doi.org/10.1038/nphys2286.

Kim, D., Li, Q., Syers, P., Butch, N.P., Paglione, J., Sarma, S.D., Fuhrer, M.S., 2012b. Intrinsic electron-phonon resistivity of Bi2Se3 in the topological regime. Phys. Rev. Lett. 109, 166801. https://doi.org/10.1103/PhysRevLett.109.166801.

Kim, D., Syers, P., Butch, N.P., Paglione, J., Fuhrer, M.S., 2013. Coherent topological transport on the surface of Bi2Se3. Nat. Commun. 4, 2040. https://doi.org/10.1038/ncomms3040.

Klitzing, K.v., Dorda, G., Pepper, M., 1980. New method for high-accuracy determination of the fine-structure constant based on quantized hall resistance. Phys. Rev. Lett. 45, 494–497. https://doi.org/10.1103/PhysRevLett.45.494.

Kong, D., Chen, Y., Cha, J.J., Zhang, Q., Analytis, J.G., Lai, K., Liu, Z., Hong, S.S., Koski, K.J., Mo, S.-K., Hussain, Z., Fisher, I.R., Shen, Z.-X., Cui, Y., 2011. Ambipolar field effect in the ternary topological insulator (Bi(x)Sb(1-x))2Te3 by composition tuning. Nat. Nanotechnol. 6, 705–709. https://doi.org/10.1038/nnano.2011.172.

Kou, X., Pan, L., Wang, J., Fan, Y., Choi, E.S., Lee, W.-L., Nie, T., Murata, K., Shao, Q., Zhang, S.-C., Wang, K.L., 2015. Metal-to-insulator switching in quantum anomalous Hall states. Nat. Commun. 6, 8474. https://doi.org/10.1038/ncomms9474.

Kurkijärvi, J., 1973. Hopping conductivity in one dimension. Phys. Rev. B 8, 922–924. https://doi.org/10.1103/PhysRevB.8.922.

Lee, P.A., 1984. Variable-range hopping in finite one-dimensional wires. Phys. Rev. Lett. 53, 2042–2045. https://doi.org/10.1103/PhysRevLett.53.2042.

Lee, D.-H., 2009. Surface states of topological insulators: the Dirac fermion in curved two-dimensional spaces. Phys. Rev. Lett. 103, 196804. https://doi.org/10.1103/PhysRevLett.103.196804.

Liao, J., Ou, Y., Feng, X., Yang, S., Lin, C., Yang, W., Wu, K., He, K., Ma, X., Xue, Q.K., Li, Y., 2015. Observation of anderson localization in ultrathin films of three-dimensional topological insulators. Phys. Rev. Lett. 114, 216601. https://doi.org/10.1103/PhysRevLett.114.216601.

Lin, C.J., He, X.Y., Liao, J., Wang, X.X., Sacksteder IV, V., Yang, W.M., Guan, T., Zhang, Q.M., Gu, L., Zhang, G.Y., Zeng, C.G., Dai, X., Wu, K.H., Li, Y.Q., 2013. Parallel field magnetoresistance in topological insulator thin films. Phys. Rev. B 88, 041307. https://doi.org/10.1103/PhysRevB.88.041307.

Linder, J., Yokoyama, T., Sudbø, A., 2009. Anomalous finite size effects on surface states in the topological insulator Bi2Se3. Phys. Rev. B 80, 205401. https://doi.org/10.1103/PhysRevB.80.205401.

Liu, C.X., Zhang, H., Yan, B., Qi, X.L., Frauenheim, T., Dai, X., Fang, Z., Zhang, S.C., 2010. Oscillatory crossover from two-dimensional to three-dimensional topological insulators. Phys. Rev. B 81, 041307. https://doi.org/10.1103/PhysRevB.81.041307.

Liu, Z.K., Jiang, J., Zhou, B., Wang, Z.J., Zhang, Y., Weng, H.M., Prabhakaran, D., Mo, S.-K., Peng, H., Dudin, P., Kim, T., Hoesch, M., Fang, Z., Dai, X., Shen, Z.X., Feng, D.L., Hussain, Z., Chen, Y.L., 2014a. A stable three-dimensional topological Dirac semimetal Cd3As2. Nat. Mater. 13, 677–681.

Liu, Z.K., Zhou, B., Zhang, Y., Wang, Z.J., Weng, H.M., Prabhakaran, D., Mo, S.-K., Shen, Z.X., Fang, Z., Dai, X., Hussain, Z., Chen, Y.L., 2014b. Discovery of a three-dimensional topological Dirac semimetal, Na3Bi. Science 343, 864–867. https://doi.org/10.1126/science.1245085.

Lu, H.Z., Shan, W.Y., Yao, W., Niu, Q., Shen, S.Q., 2010. Massive Dirac fermions and spin physics in an ultrathin film of topological insulator. Phys. Rev. B 81, 115407. https://doi.org/10.1103/PhysRevB.81.115407.

Lv, B.Q., Weng, H.M., Fu, B.B., Wang, X.P., Miao, H., Ma, J., Richard, P., Huang, X.C., Zhao, L.X., Chen, G.F., Fang, Z., Dai, X., Qian, T., Ding, H., 2015. Experimental discovery of weyl semimetal TaAs. Phys. Rev. X 5, 31013. https://doi.org/10.1103/PhysRevX.5.031013.

Martin, J., Akerman, N., Ulbricht, G., Lohmann, T., Smet, J.H., Von Klitzing, K., Yacoby, A., 2008. Observation of electron-hole puddles in graphene using a scanning single-electron transistor. Nat. Phys. 4, 144–148. https://doi.org/10.1038/nphys781.

Mendez, E.E., Esaki, L., Chang, L.L., 1985. Quantum hall effect in a two-dimensional electron-hole gas. Phys. Rev. Lett. 55, 2216–2219. https://doi.org/10.1103/PhysRevLett.55.2216.

Miao, F., Wijeratne, S., Zhang, Y., Coskun, U.C., Bao, W., Lau, C.N., 2007. Phase-coherent transport in graphene quantum billiards. Science 317, 1530–1533. https://doi.org/10.1126/science.1144359.

Minot, E.D., Yaish, Y., Sazonova, V., McEuen, P.L., 2004. Determination of electron orbital magnetic moments in carbon nanotubes. Nature 428, 536–539. https://doi.org/10.1038/nature02425.

Morimoto, T., Furusaki, A., Nagaosa, N., 2015a. Charge and spin transport in edge channels of a $\nu = 0$ quantum hall system on the surface of topological insulators. Phys. Rev. Lett. 114, 146803. https://doi.org/10.1103/PhysRevLett.114.146803.

Morimoto, T., Furusaki, A., Nagaosa, N., 2015b. Topological magnetoelectric effects in thin films of topological insulators. Phys. Rev. B 92, 085113. https://doi.org/10.1103/PhysRevB.92.085113.

Nam, H., Xu, Y., Miotkowski, I., Tian, J., Chen, Y.P., Liu, C., Hasan, M.Z., Zhu, W., Fiete, G.A., Shih, C.K., 2019. Microscopic investigation of Bi2-xSbxTe3-ySey systems: on the origin of a robust intrinsic topological insulator. J. Phys. Chem. Solid 128, 251–257. https://doi.org/10.1016/j.jpcs.2017.10.026.

Nichele, F., Pal, A.N., Pietsch, P., Ihn, T., Ensslin, K., Charpentier, C., Wegscheider, W., 2014. Insulating state and giant nonlocal response in an inas/gasb quantum well in the quantum hall regime. Phys. Rev. Lett. 112, 036802. https://doi.org/10.1103/PhysRevLett.112.036802.

Nilsson, J., Neto, A.H.C., Guinea, F., Peres, N.M.R., 2006. Electronic properties of graphene multilayers. Phys. Rev. Lett. 97, 266801. https://doi.org/10.1103/PhysRevLett.97.266801.

Nolas, G.S., Jeffrey Sharp, J.G., 2013. Thermoelectrics: Basic Principles and New Materials Developments. vol. 45 Springer Science & Business Media.

Novoselov, K.S., Geim, A.K., Morozov, S.V., Jiang, D., Zhang, Y., Dubonos, S.V., Grigorieva, I.V., Firsov, A.A., 2004. Electric field effect in atomically thin carbon films. Science 306, 666–669.

Novoselov, K.S., Geim, A.K., Morozov, S.V., Jiang, D., Katsnelson, M.I., Grigorieva, I.V., Dubonos, S.V., Firsov, A.A., 2005. Two-dimensional gas of massless Dirac fermions in graphene. Nature 438, 197–200. https://doi.org/10.1038/nature04233.

Qi, X.-L., Zhang, S.-C., 2011. Topological insulators and superconductors. Rev. Mod. Phys. 83, 1057–1110. https://doi.org/10.1103/RevModPhys.83.1057.

Qi, X.L., Hughes, T.L., Zhang, S.C., 2008. Topological field theory of time-reversal invariant insulators. Phys. Rev. B 78, 195424. https://doi.org/10.1103/PhysRevB.78.195424.

Qu, D.-X., Hor, Y.S., Xiong, J., Cava, R.J., Ong, N.P., 2010. Quantum oscillations and hall anomaly of surface states in the topological insulator Bi2Te3. Science 329, 821–824. https://doi.org/10.1126/science.1189792.

Ren, Z., Taskin, A.A., Sasaki, S., Segawa, K., Ando, Y., 2010. Large bulk resistivity and surface quantum oscillations in the topological insulator Bi2Te2Se. Phys. Rev. B 82, 241306. https://doi.org/10.1103/PhysRevB.82.241306.

Seradjeh, B., Moore, J.E., Franz, M., 2009. Exciton condensation and charge fractionalization in a topological insulator film. Phys. Rev. Lett. 103, 066402. https://doi.org/10.1103/PhysRevLett.103.066402.

Skinner, B., Chen, T., Shklovskii, B.I., 2013. Effects of bulk charged impurities on the bulk and surface transport in three-dimensional topological insulators. J. Exp. Theor. Phys. 117, 579–592. https://doi.org/10.1134/S1063776113110150.

Suzuki, K., Miyashita, S., Hirayama, Y., 2003. Transport properties in asymmetric InAs/AlSb/GaSb electron-hole hybridized systems. Phys. Rev. B 67, 195319. https://doi.org/10.1103/PhysRevB.67.195319.

Takashina, K., Nicholas, R.J., Kardynal, B., Mason, N.J., Maude, D.K., Portal, J.C., 2003. Insulating states of a broken-gap two-dimensional electron-hole system. Phys. Rev. B 68, 235303. https://doi.org/10.1103/PhysRevB.68.235303.

Tan, Y.-W., Zhang, Y., Bolotin, K., Zhao, Y., Adam, S., Hwang, E.H., Das Sarma, S., Stormer, H.L., Kim, P., 2007. Measurement of scattering rate and minimum conductivity in graphene. Phys. Rev. Lett. 99, 246803. https://doi.org/10.1103/PhysRevLett.99.246803.

Tang, F., Po, H.C., Vishwanath, A., Wan, X., 2019. Comprehensive search for topological materials using symmetry indicators. Nature 566, 486–489. https://doi.org/10.1038/s41586-019-0937-5.

Taskin, A.A., Ando, Y., 2011. Berry phase of nonideal Dirac fermions in topological insulators. Phys. Rev. B 84, 035301. https://doi.org/10.1103/PhysRevB.84.035301.

Taskin, A.A., Ren, Z., Sasaki, S., Segawa, K., Ando, Y., 2011. Observation of dirac holes and electrons in a topological insulator. Phys. Rev. Lett. 107, 016801. https://doi.org/10.1103/PhysRevLett.107.016801.

Taskin, A.A., Legg, H.F., Yang, F., Sasaki, S., Kanai, Y., Matsumoto, K., Rosch, A., Ando, Y., 2017. Planar Hall effect from the surface of topological insulators. Nat. Commun. 8, 1340. https://doi.org/10.1038/s41467-017-01474-8.

Thouless, D.J., Kohmoto, M., Nightingale, M.P., den Nijs, M., 1982. Quantized hall conductance in a two-dimensional periodic potential. Phys. Rev. Lett. 49, 405–408. https://doi.org/10.1103/PhysRevLett.49.405.

Tilahun, D., Lee, B., Hankiewicz, E.M., MacDonald, A.H., 2011. Quantum hall superfluids in topological insulator thin films. Phys. Rev. Lett. 107, 246401. https://doi.org/10.1103/PhysRevLett.107.246401.

Vafek, O., 2011. Quantum Hall effect in a singly and doubly connected three-dimensional topological insulator. Phys. Rev. B 84, 245417. https://doi.org/10.1103/PhysRevB.84.245417.

Vergniory, M.G., Elcoro, L., Felser, C., Regnault, N., Bernevig, B.A., Wang, Z., 2019. A complete catalogue of high-quality topological materials. Nature 566, 480–485. https://doi.org/10.1038/s41586-019-0954-4.

Wang, J., Lian, B., Qi, X.-L., Zhang, S.-C., 2015. Quantized topological magnetoelectric effect of the zero-plateau quantum anomalous Hall state. Phys. Rev. B 92, 081107. https://doi.org/10.1103/PhysRevB.92.081107.

Wolgast, S., Kurdak, Ç., Sun, K., Allen, J.W., Kim, D.-J., Fisk, Z., 2013. Low-temperature surface conduction in the Kondo insulator SmB6. Phys. Rev. B 88, 180405. https://doi.org/10.1103/PhysRevB.88.180405.

Xia, B., Ren, P., Sulaev, A., Liu, P., Shen, S.Q., Wang, L., 2013. Indications of surface-dominated transport in single crystalline nanoflake devices of topological insulator Bi1.5Sb0.5Te 1.8Se1.2. Phys. Rev. B 87, 085442. https://doi.org/10.1103/PhysRevB.87.085442.

Xiong, J., Petersen, A.C., Qu, D., Hor, Y.S., Cava, R.J., Ong, N.P., 2012a. Quantum oscillations in a topological insulator Bi 2Te 2Se with large bulk resistivity (6 Ω cm). Phys. E: Low-Dimens. Syst. Nanostructures 44, 917–920. https://doi.org/10.1016/j.physe.2011.09.011.

Xiong, J., Luo, Y., Khoo, Y., Jia, S., Cava, R., Ong, N., 2012b. High-field Shubnikov–de Haas oscillations in the topological insulator Bi2Te2Se. Phys. Rev. B 86, 045314. https://doi.org/10.1103/PhysRevB.86.045314.

Xu, Y., Miotkowski, I., Liu, C., Tian, J., Nam, H., Alidoust, N., Hu, J., Shih, C.-K., Hasan, M.Z., Chen, Y.P., 2014. Observation of topological surface state quantum Hall effect in an intrinsic three-dimensional topological insulator. Nat. Phys. 10, 956–963. https://doi.org/10.1038/nphys3140.

Xu, S.Y., Belopolski, I., Alidoust, N., Neupane, M., Bian, G., Zhang, C., Sankar, R., Chang, G., Yuan, Z., Lee, C.C., Huang, S.M., Zheng, H., Ma, J., Sanchez, D.S., Wang, B.K., Bansil, A., Chou, F., Shibayev, P.P., Lin, H., Jia, S., Hasan, M.Z., 2015. Discovery of a Weyl fermion semimetal and topological Fermi arcs. Science 349, 613–617. https://doi.org/10.1126/science.aaa9297.

Xu, Y., Miotkowski, I., Chen, Y.P., 2016. Quantum transport of two-species Dirac fermions in dual-gated three-dimensional topological insulators. Nat. Commun. 7, 11434. https://doi.org/10.1038/ncomms11434.

Yu, R., Zhang, W., Zhang, H.-J., Zhang, S.-C., Dai, X., Fang, Z., 2010. Quantized anomalous Hall effect in magnetic topological insulators. Science 329, 61–64. https://doi.org/10.1126/science.1187485.

Zhang, Y., Tan, Y.-W., Stormer, H.L., Kim, P., 2005. Experimental observation of the quantum Hall effect and Berry's phase in graphene. Nature 438, 201–204. https://doi.org/10.1038/nature04235.

Zhang, Y., He, K., Chang, C.-Z., Song, C.-L., Wang, L.-L., Chen, X., Jia, J.-F., Fang, Z., Dai, X., Shan, W.-Y., Shen, S.-Q., Niu, Q., Qi, X.-L., Zhang, S.-C., Ma, X.-C., Xue, Q.-K., 2010. Crossover of the three-dimensional topological insulator Bi2Se3 to the two-dimensional limit. Nat. Phys. 6, 584–588.

Zhang, Y.-Y., Wang, X.-R., Xie, X.C., 2012. Three-dimensional topological insulator in a magnetic field: chiral side surface states and quantized Hall conductance. J. Phys. Condens. Matter 24, 015004. https://doi.org/10.1088/0953-8984/24/1/015004.

Zyuzin, A.A., Hook, M.D., Burkov, A.A., 2011. Parallel magnetic field driven quantum phase transition in a thin topological insulator film. Phys. Rev. B 83, 245428. https://doi.org/10.1103/PhysRevB.83.245428.